Mobility of continental mantle: Evidence from postseismic geodetic observations following the 1992 Landers earthquake

Fred F. Pollitz

Department of Geology, University of California, Davis

Gilles Peltzer

Jet Propulsion Laboratory, Pasadena, California

Roland Bürgmann

Department of Geology and Geophysics, University of California, Berkeley

Abstract. The crust around the rupture zone of the 1992 Landers earthquake has continued to deform in the years following the earthquake at rates ~3 times greater than pre-earthquake rates. We use a combination of Global Positioning System (GPS) and synthetic aperture radar (InSAR) data collected during a ~3-year epoch following the earthquake in order to investigate postseismic mechanisms responsible for the high transient velocities. In order to maximize the potential signal from viscoelastic relaxation we evaluate and model postseismic relaxation following the first few months of documented accelerated deformation. The combination of GPS and InSAR data allows us to establish viscoelastic relaxation of the lower crust and upper mantle as the dominant postseismic process and to discriminate among possible viscoelastic models. The data particularly require the presence of a highly ductile uppermost mantle beneath the central Mojave Domain, with temperature between the wet and dry basalt solidus. This is consistent with independent seismic and geochemical inferences of a regionally warm uppermost mantle. Further consideration of seismic velocity variations in conjunction with faulting patterns within the Mojave Desert suggests that the primary faulting characteristics of the Mojave Desert, namely, the pervasive late Cenozoic deformation within the Eastern California Shear Zone versus the near absence of faults in the Western Mojave Domain, are controlled by the rheology of the uppermost mantle.

1. Introduction

The strength of the Earth's lithosphere is of central importance for understanding mountain building [*Chery et al.*, 1991], continental rifting [e.g., *Buck*, 1991; *Zeyen et al.*, 1997], and the propagation of stresses through continental lithosphere [*Kusznir*, 1982]. Continental lithosphere is thought to be characterized by a brittle upper crust, a ductile and weak lower crust, and a ductile but much stronger mantle lithosphere. This picture is based on the correlation of cutoff depth in continental seismicity with the onset of thermally activated processes in crustal materials [*Sibson*, 1982], the seismic and geological evidence for a weak lower crust [*Kay and Kay*, 1981; *Hacker et al.*, 1992; *Brocher et al.*, 1994], and the mechanical properties of the primary constituents of the crust and upper mantle [*Brace and Kohlstedt*, 1980], and it is often summarized in terms of strength envelopes [*Brace and Kohlstedt*, 1980; *Molnar and Tapponier*, 1981; *Chen and Molnar*, 1983]. A relatively cool geotherm is expected to result in a less ductile, "strong" uppermost mantle, as occasionally directly manifested by mantle seismicity [*Chen and Molnar*, 1983]. The expectation that higher-than-normal temperatures in themantle should increase its ductility is consistent with the association of high topography with warm and likely convecting mantle [e.g., *Jones*

et al., 1996; *Wernicke et al.*, 1996; *Lithgow-Bertelloni and Silver*, 1998] and the association of highly thickened crust with thermally weakened mantle [*Chery et al.*, 1991; *Wdowinski and Bock*, 1994].

A direct way of characterizing the ductility of the uppermost mantle is to infer its viscosity from geodetic observations made after large earthquakes. This method is based on the supposition that the coseismic stresses generated by an earthquake cannot be sustained by the ductile lower crust and upper mantle, leading to postseismic relaxation of these materials which is, in turn, transferred to the upper crust, producing observable transient geodetic signals. Such signals have a predictable, essentially space- and time-transgressive diffusive behavior [e.g., *Bott and Dean*, 1973; *Nur and Mavko*, 1974; *Rydelek and Sacks*, 1990; *Cohen*, 1992; *Pollitz*, 1997] consistent with observations in a number of cases. Triangulation and leveling data collected after large earthquakes in Japan and California have been successfully (but not uniquely) explained in terms of postseismic relaxation behavior [e.g., *Thatcher et al.*, 1980; *Miyashita*, 1987; *Tabei*, 1989; *Pollitz and Sacks*, 1992, 1994]. The large uncertainties, infrequent time sampling, and configuration of triangulation and leveling networks have made it difficult to distinguish between broadscale, deep relaxation processes versus localized crustal afterslip. Moreover, for the special case of a very long strike-slip fault, both deep afterslip and deep viscoelastic flow can produce the same horizontal surface deformation [*Savage*, 1990]. Horizontal geodetic data complemented by vertical data, however, remove this ambiguity and allow discrimination between afterslip and viscoelastic flow mechanisms for a rupture of finite dimension.

Uppermost mantle viscosity is thought to play a fundamental role in the style of regional crustal deformation in both the short and long term [e.g., *Furlong et al.*, 1989; *Kusznir*, 1991; *Jones et al.*, 1996], yet it has not been directly estimated even in relatively well-monitored regions because of nonuniqueness in interpreting available geodetic data as well as the paucity of seismic sources of sufficient strength to excite observable postseismic signals. For example, Global Positioning System (GPS) and leveling data around the rupture zone of the M_w = 6.9 1989 Loma Prieta earthquake were recently considered by *Pollitz et al.* [1998] in order to establish the possible importance of various postseismic processes. Interpretation of this postseismic velocity field strongly suggests that shallow afterslip is the dominant postseismic process. Although the data also appear to resolve a tangible signal from deep viscoelastic relaxation, the trade-offs with relatively shallow afterslip are substantial and there is not enough resolution to distinguish among even grossly different (but equally viable) viscoelastic stratifications such as strong versus weak uppermost mantle. A study of geodetic velocities collected in the 2 years after the M_w = 6.7 Northridge earthquake [*Donnellan and Lyzenga*, 1998] confronts similar difficulties. Near-field horizontal and vertical GPS measurements (and far-field measurements at one site) point to shallow afterslip as the dominant postseismic process. Although lower crustal viscoelastic relaxation alone is ruled out by the data, it is possible that a slow (and as yet undetectable) viscoelastic relaxation signal is imposed on a larger afterslip signal. Thus, in both the post-Loma Prieta and post-Northridge cases, the

domination of shallow afterslip in the immediate (2–5 years) postseismic epoch, as well as the relatively small size of these earthquakes and the distribution and type of data, have made detection of a deep viscoelastic relaxation signal problematical.

The M_w = 7.3 1992 Landers earthquake, a larger event, involved an average of 3–4 m of right-lateral slip on long-dormant faults of total length ~80 km traversing the Eastern California Shear Zone (ECSZ) in the central Mojave Domain [*Hart et al.*, 1993; *Sieh et al.*, 1993] (Figures 1a and 2). In the months and years following the earthquake the epicentral region has been monitored with GPS networks, trilateration arrays, creep meters, and interferometric processing of synthetic aperture radar (InSAR) data. These types of data (covering time periods ranging from several days to years) have been previously considered byseveral investigators, and several postseismic processes havebeen proposed. These include (1) fault zone collapse [*Massonnet et al.*, 1996], (2) afterslip [*Shen et al.*, 1994; *Massonnet et al.*, 1994; *Wdowinski et al.*, 1997; *Savage and Svarc*, 1997], (3) poroelastic rebound [*Peltzer et al.*, 1996, 1998], and (4) viscoelastic relaxation of the lower crust and upper mantle [*Ivins*, 1996; *Yu et al.*, 1996; *Deng et al.*, 1998]. The studies by *Massonnet et al.* [1996], *Peltzer et al.* [1996], and *Peltzer et al.* [1998] utilize InSAR data alone; that of *Wdowinski et al.* [1997] utilizes GPS data recorded by remote (>65 km) stations of the southern California Permanent GPS Geodetic array (PGGA), and the remaining studies utilize campaign GPS measurements. With the exception of the continuous GPS measurements at remote stations of the PGGA, the GPS studies have provided no or poor estimates of vertical deformation. Bythe same token, the InSAR range change is shaped primarily by the vertical displacement field.

Both vertical and horizontal deformation information together are critical for addressing uniqueness in interpretation of postseismic processes. In this paper we analyze a joint data set consisting of GPS and InSAR data collected in the 3 years after the Landers earthquake. This combination proves to be effective in discriminating among the above candidate postseismic processes. We find that the long-wavelength (horizontal scale larger than ~5 km) postseismic deformation pattern is dominated by deep viscoelastic relaxation. This data combination is also effective in discriminating among different models of regional viscoelastic stratification, and we infer a very weak uppermost mantle beneath the central Mojave Desert.

Viscosity structure provides important constraints on the physical state of the crust and upper mantle. The Mojave Desert lies at the southwestern edge of the Basin and Range province, which has experienced substantial horizontal extension over the past 20 Myr [*Stewart*, 1978], and it encompasses the transition from rifting to strike-slip faulting within the modern San Andreas fault system. Intense debate centers on whether significant thinning or erosion of the mantle lithosphere has occurred there during the Cenozoic, either during the epoch of low-angle Farallon plate subduction or following the transition to a dominantly strike-slip Pacific-North America plate boundary zone. Geochemical analyses of mantle-derived alkali basalts in the late Cenozoic volcanic fields of the Mojave Desert yield a strong similarity to Pacific mid-ocean ridge basalt (MORB) source rocks [*Glazner et al.*, 1991], suggesting the existence of an underlying asthenosphere no

deeper than 50–70 km [*Livaccari and Perry*, 1993]. Consideration of the elevation difference between the northern and southern Basin and Range province, however, suggests a relatively cool upper mantle beneath the southern Basin and Range and eastern Mojave Desert [*Saltus and Thompson*, 1995]. The former view is supported by upper mantle seismic velocities in the eastern half of the Mojave Desert (Figure 1b) [*Humphreys and Dueker*, 1994], while the latter view is supported by the crustal geotherm derived by *Williams* [1996]. The present study may shed further light on the state of the uppermost mantle beneath the east central Mojave Desert.

In subsequent sections we present the data, give arguments for the dominance of viscoelastic relaxation over other possible postseismic processes, and discuss the implications of our estimate of regional mantle viscosity.

2. Data Set

This study utilizes both GPS and InSAR collected in the 3 years following the June 28, 1992, Landers earthquake (Plates 1a and 1c). The GPS data (Table 1) consist of horizontal velocity vectors and corresponding covariance matrices $\mathbf{C}_h$ determined over the following networks and occupation times: (1) 14 sites released by the Southern California Earthquake Center (SCEC) and analyzed by University of California, Los Angeles, for the period September/November 1992 to December 1995 (SCEC Release 2, 1998, available at http://www.scecdc.scec.org/group_e/ release.v2), and (2) 12 U.S. Geological Survey (USGS) sites analyzed by *Savage and Svarc* [1997] for the period November 1992 to December 1995 (Emerson transect). All horizontal velocities are with respect to the fixed site GOLD (Table 1). These two GPS data sources combined provide good coverage (primarily west of the rupture zone) of average horizontal velocity in the near field (within 30 km of the rupture zones), intermediate field (30–60 km), and far field (> 60 km). In Table 1 we separate these data into near-field and far-field categories. The InSAR data represent total range change over the period September 27, 1992, to January 23, 1996. The interferogram was computed using pairs of SAR images provided by the European Space Agency, and it contains a substantial vertical displacement signal in both the near field and intermediate field. Further details are given by *Peltzer et al.* [1998]. Although postseismic observations beginning within days of the Landers earthquake are available [e.g., *Shen et al.*, 1994; *Massonnet et al.*, 1994; *Savage and Svarc*, 1997], we restrict attention to postseismic observations made in September 1992 and thereafter in order to avoid complications associated with possible rapid afterslip or relaxation during the first three months after the earthquake [*Shen et al.*, 1994; *Massonnet et al.*, 1994; *Ivins*, 1996; *Yu et al.*, 1996].

Formal error estimates are readily available for the GPS data in the form of a covariance matrix $\mathbf{C}_h$ provided by J. Svarc (personal communication, 1998) and SCEC Release 2. A covariance matrix $\mathbf{C}_R$ carrying information about statistical correlations of errors among the InSAR range change estimates is not available. Although this issue is not critical for our study (we do not require absolute error estimates of any data subset for our analysis), we have nevertheless taken a first-order

approach in addressing this issue. We have defined a covariance matrix $\mathbf{C}_R$ for the InSAR image designed to accommodate small uncertainties in both regional tilt and local observation error.Small unknown errors in orbital position translate into an unknown additional regional tilt upon forming phase differenceimages in InSAR analysis. We account for possible correlations between the observed and calculated range change images due to possible broadscale regional tilt. We represent range change R over a rectangular $x - y$ grid as $R(x,y) = R_0(x,y) + a\,x + b\,y + c(x,y)$, where R_0 is deterministic signal, a and b represent unknown tilt, and c represents local noise.Assuming in a statistical sense Var $a = \sigma_a^2$, Var $b = \sigma_b^2$, and Var $c = \sigma_c^2$, and that a, b, and c have zero expectation value and are uncorrelated with one another yields the covariance between two points (x_1,y_1) and (x_2,y_2) in the interferogram:

$$\mathbf{C}_R(x_1,y_1;x_2,y_2) = \sigma_a^2\, x_1\, x_2 + \sigma_b^2\, y_1\, y_2 + \sigma_c^2\,. \qquad (1)$$

The full covariance matrix includes the covariances between each measurement in the interferogram. This covariance matrix with values $\sigma_a = \sigma_b = 1.5 \times 10^{-7}/(3.31\ \text{years})$ and $\sigma_c = 0.75\text{cm}/(3.31\ \text{years})$ will be subsequently employed in equation (6).

3. Interpretation

3.1. Dominance of Deep Viscoelastic Relaxation

A whole array of postseismic processes likely contribute to varying degrees to the observed postseismic deformation field. The GPS and InSAR measurements may be interpreted as the product of (1) fault zone collapse [*Massonnet et al.*, 1996], (2) afterslip on or beneath the Landers seismogenic rupture zone [*Shen et al.* , 1994; *Savage and Svarc*, 1997], (3) poroelastic rebound [*Peltzer et al.*, 1996, 1998], (4) viscoelastic relaxation of the lower crust and upper mantle driven by the coseismic stress changes [*Ivins*, 1996; *Yu et al.*, 1996; *Deng et al.*, 1998], and (5) interseismic strain accumulation.

Interseismic strain accumulation is modeled here using the slip-at-depth model specified by *Feigl et al.* [1993] and Table 3 of *Savage and Svarc* [1997]. Figure3a shows the strike-slip fault traces used, and Figure 3b shows the interseismic velocity field calculated at the 26 GPS sites relative to a fixed Goldstone, as tabulated in Table 1. The interseismic velocity field relative to a fixed Goldstone does not, with the exception of PIN1, exceed 6 mm/yr and is generally a fraction of the observed relative velocity (Table 1). This is also seen by comparison of Figure 3b and Plate 1c.

The observed postseismic velocity field is therefore shaped primarily by processes which are unique to the Landers postseismic epoch. These are processes 1 to 4 above, and we now evaluate the relative merits of these processes. Poroelastic rebound alone, assuming drained pore fluid conditions over the entire region following the Landers earthquake (with values of 0.27 and 0.31 for the drained and undrained Poisson's ratio, respectively [*Peltzer et al.*, 1998]), predicts horizontal velocities of only very small magnitude and thus cannot explain the observed GPS velocity field, even if it explains remarkably well the observed InSAR image (Plate 2b). It appears to be a

particularly important postseismic process around localized fault bends where sharp gradients in range change pattern are observed (Plate 1a). Afterslip alone, if it does not extend deeper than 30 km depth, can adequately explain the near-field GPS velocity field, as demonstrated by *Savage and Svarc* [1997] using the Emerson transect data, but the predictions of their model are practically anticorrelated with the observed InSAR image (Plate 2a). A combination of poroelastic rebound and afterslip can adequately explain the near-field GPS velocity field and the northern portion of the InSAR image (Plate 2c). Neither the persistence of significant horizontal postseismic deformation up to 100 km from the rupture zones (Plate 1c) nor the southern portion of the InSAR image (Plate 1a), however, can be explained with this combination. Fault zone collapse alone is similarly unable to produce the significant far-field deformation which is observed. If postseismic relaxation plus interseismic strain accumulation are invoked to explain the far-field observations, then we find that they are sufficient to explain the near-field observations as well. These arguments suggest at most minor contributions of fault zone collapse, poroelastic rebound, or afterslip to the long-wavelength postseismic deformation pattern during the 3-year epoch beginning 3-5 months after the Landers earthquake, and we shall henceforth focus on postseismic relaxation and interseismic strain accumulation only.

3.2. Viscoelastic Stratification of Central Mojave Domain

We intend to construct a model of the regional viscoelastic stratification which satisfactorily explains both the horizontal GPS and InSAR range change observations during the Landers postseismic epoch. In order to clarify the importance of various subsets of the data we shall subdivide the total data set (Plates 1a and 1c) into four distinct subsets reflecting the different influences of data type and distance from the rupture zones (i.e., near-field versus far-field). In order to evaluate misfit with respect to these data subsets we shall present the forward problem in terms of the summed effects of interseismic velocity plus viscoelastic relaxation of the lower crust and mantle. The latter is completely specified by the Landers coseismic rupture model, which is assumed known, elastic stratification (also assumed known), and unknown viscoelastic stratification (which includes the influence of the initial stress field; see section 5.1). After defining our model parameter space, we shall evaluate misfit of these data subsets within this model space and discuss which combinations of viscoelastic parameters yield the best fit to all data considered.

Let t_1 and t_2 denote the start and end time, respectively, of repeated geodetic surveys. We work with 26 horizontal GPS velocity vectors $\mathbf{v}_h(\mathbf{r}_i;t_1,t_2)$ ($i = 1,2,\cdots,26$) and InSAR range change pattern $R(\mathbf{r};t_1,t_2)$ covering a continuous 90×70 km^2 area. Predicted horizontal velocity and range change are expressed as follows:

$$\mathbf{v}(\mathbf{r};t_1,t_2) = -\frac{1}{t_1-t_2}\left[\int_{\substack{\text{Landers}\\ \text{earthquake}\\ \text{fault}}} \mathbf{G}^{(ps)}(\mathbf{r},\mathbf{r}_0;t_1,t_2)\, s(\mathbf{r}_0)\, d^2\mathbf{r}_0 + \int_{\substack{\text{interseismic}\\ \text{slipping}\\ \text{segments}}} \mathbf{G}^{(is)}(\mathbf{r},\mathbf{r}_0;t_1,t_2)\, d(\mathbf{r}_0)\, d^2\mathbf{r}_0\right] \qquad (2)$$

$$\mathbf{v}_h(\mathbf{r};t_1,t_2) = \mathbf{v}(\mathbf{r};t_1,t_2) - \left[\mathbf{v}(\mathbf{r};t_1,t_2)\cdot\hat{\mathbf{z}}\right]\hat{\mathbf{z}} \quad (3)$$

$$R(\mathbf{r};t_1,t_2) = \mathbf{v}(\mathbf{r};t_1,t_2)\cdot\hat{\gamma}\,. \quad (4)$$

Equation (2) represents the vector velocity $\mathbf{v}$ as a sum of postseismic relaxation and interseismic strain accumulation, respectively, each expressed as a convolution of a Greens function and slip defined over appropriate dislocation planes. For the postseismic component the Landers earthquake fault area and coseismic right-lateral strike-slip distribution $s(\mathbf{r}_0)$ are prescribed by *Wald and Heaton* [1994]. For the Big Bear segment we use a fault length of 12 km striking N50°E, a dip of 90°, a width of 8 km (7–15 km depth range), a uniform slip of 2.50 m, and a total seismic moment of 9×10^{18} N m. These values are appropriate for the main shock of the Big Bear sequence [*Jones and Helmberger*, 1993]. The Greens function $\mathbf{G}^{(ps)}$ is prescribed by *Pollitz* [1997]. For the interseismic component the distribution of deep slipping segments and the corresponding velocity distribution $d(\mathbf{r}_0)$ are prescribed by *Feigl et al.* [1993] and Table 3 of *Savage and Svarc* [1997], and the Greens function $\mathbf{G}^{(is)}$ is prescribed by *Okada* [1985] (a half-space elastic mediumis appropriate for calculating the interseismic componentbecause such a medium is assumed by *Feigl et al.* [1993] in order to match regional geodetic surface displacements). The unit vectors $\hat{\mathbf{z}}$ and $\hat{\gamma}$ point toward the locally up direction and the line-of-sight direction of the satellite used in the InSAR analysis, respectively. The azimuth $\hat{\gamma}$ in local east-north-up coordinatesis (0.381, -0.088, 0.920) [*European Space Agency*, 1992].

Given a fault model of the Landers earthquake, surface deformation resulting from viscoelastic relaxation of the lower crust and mantle is determined by the viscoelastic stratification (Figure 4). In our modeling, we choose elastic parameters appropriate for the region [*Qu et al.*, 1994, Table 1] and allow the following parameters to be variable: η_c, η_{m1}, and η_{m2} (lower crust, uppermost mantle, and deeper mantle viscosity, respectively) and μ' (the long-term strength of the lower crust) [*Cohen*, 1982; *Ivins and Sammis*, 1996]. A value $\mu' = 0$ corresponds to a Maxwell viscoelastic fluid, and a finite value of μ' corresponds to a material which can maintain a certain amount of shear stress, nominally a fraction of its short-term strength, over indefinitely long periods of time. A significantly nonzero μ' in the northeast Iceland lower crust was strongly suggested in the postrifting study of *Pollitz and Sacks* [1996] around the Krafla rift. This parameter is found to exert a moderate influence on the present results as well. A viscosity decrease of about one order of magnitude within the top 100 km of the mantle is dictated by the increase in dislocation mobility of olivine with depth [*Karato et al.*, 1993]. If, as is suggested by isotopic compositions, asthenosphere is present no deeper than 50–70 km depth in the area [*Livaccari and Perry*, 1993], then the mantle viscosity below the dehydration boundary (~65 km depth, where melt extraction alters the water content [*Hirth and Kohlstedt*, 1996]) should be $\sim 10^{18}$ Pa s, about a factor of 5 lower than the mantle viscosity that would be inferred in our study if an isoviscous mantle were assumed (section 4.1). As will be justified shortly, we represented this viscosity decrease by prescribing a mantle viscosity ratio $\eta_{m1}/\eta_{m2} = 3$, i.e., a threefold decrease in mantle viscosity at 50 km depth.

Values of $\mu' =$ 6, 12, 18, 24, and 30 GPa were considered and evaluated. Best results were obtained with $\mu' = 12$ GPa, but our main conclusions are robust with respect to the choice of μ'. We shall therefore restrict attention to the two cases: $\mu' =$ 0 and $\mu' = 12$ GPa. We calculated $\mathbf{v}_h$ and R for these values of μ' and over the range $\eta_c / \eta_{m1} = 3.6 \times 10^{-2}$–$10^{1}$ and $\eta_{m1} = 10^{18} - 10^{20}$ Pa s. In order to compare modeled and observed deformation, we define misfit $\chi^2_{(j)}$ for each of four data subsets [*Savage and Svarc*, 1997; *Peltzer et al.*, 1998; SCEC Release 2], far-field SCEC GPS (j=1), near-field SCEC GPS (j=2), USGS GPS (j=3), and JPL InSAR (j=4) as follows:

$$\chi^2_{(1,2,\text{ or }3)} = (\Delta[\mathbf{v}_h])^T \, \mathbf{C}^{-1}_h \, (\Delta[\mathbf{v}_h]) \quad (5)$$

$$\chi^2_{(4)} = \left[\Delta[R(\mathbf{r};t_1,t_2)] + \text{const}\right]^T \mathbf{C}^{-1}_R \left[\Delta[R(\mathbf{r};t_1,t_2)] + \text{const}\right], \quad (6)$$

where $\Delta[\,]$ denotes the difference between a calculated and observed quantity and $\mathbf{C}_h$ and $\mathbf{C}_R$ are covariance matrices of GPS and InSAR data, respectively. Far-field and near-field subsets of the SCEC GPS data set are realized by retaining nonzero $\mathbf{v}_h$ in (5) according to whether the GPS site lies outside of or within, respectively, the small boxed region of Plate 1c. In order to employ consistent reference frames for all calculations and observations all calculated and observed horizontal deformation is referred to the fixed site GOLD (Table 1) by subtracting its observed and modelled velocity from all observed and modelled site velocities, respectively. Mathematically, this means that the adjustments

$$\mathbf{v}_h(\mathbf{r}_i;t_1,t_2)_{\text{obs}} \longrightarrow \mathbf{v}_h(\mathbf{r}_i;t_1,t_2)_{\text{obs}} - \mathbf{v}(\text{Goldstone};t_1,t_2)_{\text{obs}} \quad (7)$$

$$\mathbf{v}_h(\mathbf{r}_i;t_1,t_2)_{\text{cal}} \longrightarrow \mathbf{v}_h(\mathbf{r}_i;t_1,t_2)_{\text{cal}} - \mathbf{v}(\text{Goldstone};t_1,t_2)_{\text{cal}} \quad (8)$$

have been performed for all horizontal deformation discussed in this report. Also, the constant in (6) is always chosen such that the mean of the bracketed quantity is zero.

Misfit patterns $\log_{10}\chi^2_{(j)}$ (j = 1,2,3,4) for $\mu' = 12$ GPa are shown in Figure 5 (left). Corresponding results for a Maxwell viscoelastic fluid lower crust ($\mu' = 0$) are shown in Figure 5 (right). We note that for each data subset j, there is a local minimum in $\chi^2_{(j)}$ in the neighborhood of the following model (indicated by solid circles in Figure 5):

$\eta_{m1} = 8.0 \times 10^{18}$ Pa s
$\eta_{m2} = 2.7 \times 10^{18}$ Pa s
$\eta_c / \eta_{m1} = 2.0$
$\mu' = 12$ GPa

(Mojave Block model). Calculated range change and horizontal velocity field for the Mojave Block model are shown in Plates 1b and 1c. This simple viscoelastic coupling model duplicates the main long-wavelength features of both the range change and horizontal velocity fields. The calculated range change (Plate 1b) does not include any tilt, and we found that a substantial portion of the remaining misfit could be explained by a tilt of 20 mm per geocentric degree @S60°W.

We now consider which other models perform comparably with this one. Acceptable models must provide a good fit to all data subsets simultaneously. The most straightforward way to evaluate the suite of models would be to consider the statistic

$$\chi^2 = \sum_{j=1}^{4} \chi^2_{(j)} \, . \qquad (9)$$

Unfortunately, this measure is sensitive to the absolute error scaling of the various data subsets. Although both the GPS and InSAR data can be fit at the level of ~80–90% variance reduction, the residual misfit of the three GPS data subsets averages between 2σ and 3σ (where σ represents one standard deviation), whereas the InSAR data are fit closer to the level of 1σ. The InSAR data are consequently grossly under-represented in χ^2 as written in (9). We choose an approach which avoids the issue of absolute error scaling. For each data subset j we consider the set of models (η_{m1},η_c,μ') such that the improvement in $\chi^2_{(j)}$ obtained by the parameter combination of the Mojave Block model is significant at the 95% or 99% confidence level. Then F_χ obeys the $F-$distribution, where F_χ is given by

$$F_\chi = -\frac{\left(\chi^2(\eta_{m1},\eta_c,\mu') - \chi^2(\text{Mojave Block model})\right)/3}{\chi^2(\text{Mojave Block model})/(N-3)} \, , \qquad (10)$$

where N is the number of independent data in data subset j. Define $(\Omega_F)_j$ to be the region in the model space such that $F_\chi < P(F\,|\,3,N)$, where $P(F\,|\,\nu_1,\nu_2)$ is defined by equation 26.6.1 of *Abramowicz and Stegun* [1984]. Finally,define Ω_F to be the intersection of the sets $(\Omega_F)_j$, i.e., that part of the model space which fits each data subset at probability level P. Since each $(\Omega_F)_j$ is independent of the absolute error scaling, Ω_F is as well, so we consider it to be a useful objective definition of the best fitting models. Figure 6 shows Ω_F at probability levels $P = 0.95$ and $P = 0.99$ at the model slices $\mu' = 12$ GPa and $\mu' = 0$. We conclude that uppermost mantle viscosity beneath the central Mojave Domain equals $8 \pm 4 \times 10^{18}$ Pa s (99% confidence interval), corresponding to a maximum characteristic relaxation time of η_{m1}/μ_m = ~3.6 years, i.e., a mobile uppermost mantle. It is noteworthy that consideration of near-field GPS data alone would render models of low μ', high η_{m1}, and low η_c plausible. Theadditional information provided by far-field GPS and near-field InSAR data rules out this possibility.

4. Discussion

4.1. End-Member Mantle Viscosity Models

We find that if the statistical analysis of section 3.2 is repeated using mantle viscosity ratios η_{m1}/η_{m2} equal to 1 and 10, sharp local minima similar to those seen in Figure 6 are obtained with a shift toward lower $\eta_{m1} = 5 \times 10^{18}$ Pa s or higher $\eta_{m1} = 1.1 \times 10^{19}$ Pa s, respectively. This is illustrated for the isoviscous mantle model $\eta_{m1} = \eta_{m2}$ in Figure 7. In both these end-member cases and for intermediate ratios (such as the Mojave Block model), average mantle viscosity within the top 40 km of the mantle is about 5×10^{18} Pa s. Regardless of the details of the viscosity decrease with depth, a low-viscosity uppermost mantle is a robust result.

Our analysis with $\eta_{m1}/\eta_{m2} = 3$ yields a low uppermost mantle viscosity η_{m1} near 8×10^{18} Pa s, but lower crustal viscosity η_c may lie near either 5×10^{18} Pa s or 2×10^{19} Pa s (based on the bimodal distribution exhibited in Figure 6). In addition, the analysis can not discriminate among low and high μ', though a nonzero $\mu' = 12$ GPa generally yields slightly smaller residual

misfits. We favor the larger possible crust-to-mantle viscosity ratio of ~2, in the Mojave block model because the local minimum in data misfit is strongest for that value. For purposes of discussion, we will consider the ratio η_c / η_{m1} and μ' fixed at the values determined for the Mojave Block model and focus on the resolution of the mantle viscosity stratification.

We may examine in greater detail two end-member models constructed with mantle viscosity contrasts of 1 and 10. Two forward models using these ratios are presented in Plate 3. The first end-member model is prescribed by $\eta_{m2} = \eta_{m1} = 6.0 \times 10^{18}$ Pa s and is found to yield a good fit to the horizontal velocity field, but it does not predict the observed substantial decrease in range change from west to east across the Johnson Valley fault (Plates 3a and 3b). From comparison with Figure 1c, the InSAR data thus favor a factor ≥ 3 decrease in mantle viscosity below 50 km depth. A decrease in mantle viscosity with depth is also suggested by the USGS Emerson transect data, where systematic misfits between observed and calculated horizontal velocities are large for $\eta_{m1} / \eta_{m2} = 1$ (Plate 3b), small for $\eta_{m1} / \eta_{m2} = 3$ (Plate 1c) and smaller still for $\eta_{m1} / \eta_{m2} = 10$ (Plate 3d). It should be noted, however, that allowance for numerous unmodeled factors could modify our predictions enough to remove the requirement for this viscosity decrease. These include (1) afterslip on the Eureka Peak and southern Johnson Valley fault segments [*Behr et al.*, 1994], (2) poroelastic rebound [*Peltzer et al.*, 1998], and (3) lateral variations in poroelastic and viscoelastic stratification. All of these may also contribute to many shorter wavelength features on the observed InSAR image (Plate 1a).

4.2. Modeling of Emerson Transect Data

As noted above, a systematic offset of about 4 mm/yr toward the southwest is apparent in the calculated vectors at the USGS Emerson transect sites on the Mojave Block model (Plate 1c). As demonstrated in Plate 3, this offset is found to increase or decrease substantially when models with smaller or larger η_{m1} / η_{m2}, respectively, are considered. Rather than use this to argue unequivocally for a sharp mantle viscosity decrease with depth, it is worthwhile to explore alternative causes. The offset could be caused by inaccuracies in calculated deformation at the reference site GOLD arising from the interseismic velocity correction or the calculated viscoelastic relaxation. The latter could result from a very different viscoelastic stratification north of the study area compared with that within the study area. All of these possibilities, however, would be expected to produce systematic offsets at all GPS sites, and the SCEC GPS sites do not exhibit the offset. Unmodeled postseismic processes on the Emerson and Camp Rock faults are another possibility. Fault-zone collapse would be expected to produce a symmetric velocity pattern with respect to the fault trace, in contrast with the uniformity of the offset. Relaxation following dip-slip coseismic motions on the Emerson and Camp Rock faults, as advocated by *Deng et al.* [1998], is another possibility, but the additional velocity produced by the suspected dip-slip components is toward the southwest, which would degrade the offset of our model even further. These considerations raise the possibility of a solid body rotation between the SCEC and USGS data sets. The two data sets have no sites in common except GOLD for the time period modeled here

(September/November 1992–1995). For a ~3-year period beginning in mid-late July 1992, the USGS data [*Savage and Svarc*, 1997] and SCEC data (SCEC Release 2) have two sites in common (in addition to GOLD): PIN1 and SANH/SAND (Table 1). The velocity vectors with respect to GOLD in the two data sets are for PIN1, -6.8 mm/yr east, 12.6 mm/yr north (SCEC) and -2.6 mm/yr east, 14.4 mm/yr north (USGS); for SANH/SAND, 9.3 mm/yr east, -9.1 mm/yr north (SCEC) and 17.3 mm/yr east, -6.0 mm/yr north (USGS). Sites GOLD and PIN1 are both continuous PGGAsites, while SANH/SAND are campaign sites. Both sets of velocities disagree by several millimeters per year. Althoughthis may be partly due to the slightly nonoverlapping time intervals involved in this comparison, this suggests sizable discrepancies between the two data sets. A reviewer (L. Hearn) has pointed out similar discrepancies at these two sites within the early postseismic epoch alone. If the discrepancies continued into the later postseismic epoch, then they may be related to the offset exhibited in Plate 1c. We will not attempt to resolve the origin of the offset in this paper, if it exists at all. In any case, the magnitude of the offset in our preferred model is fairly small, and our preferred viscoelastic model reproduces quite accurately the strain field represented by the USGS GPS data.

4.3. Temporal Variation in Effective Viscosity

A power law relationship between stress and strain rate in the upper mantle can be used to express effective viscosity η_{eff} in terms of strain rate at a given temperature:

$$\eta_{eff} \sim \dot{\varepsilon}^{(1-n)/n}, \qquad (11)$$

where $n \sim 3.5$ [*Karato and Wu*, 1993]. The large transient velocities observed in the first few months following the Landers earthquake have been interpreted in terms of very low effective viscosity $\eta_{eff} \sim 10^{17}$ Pa s [*Yu et al.*, 1996]. The fact that this estimate is much smaller than our estimate of $\eta_{eff} = 8.0 \times 10^{18}$ Pa s for the 3-year period following the initial postseismic phase may indicate (1) rapid afterslip during the initial postseismic phase [*Shen et al.*, 1994], (2) a biviscous lower crust with ~5% concentrations of oblate spherical inclusions of viscosity $3 - 4 \times 10^{15}$ Pa s [*Ivins*, 1996], or (3) a rapid decrease in crust and/or mantle strain rate with time following the earthquake, based on equation (11). Discriminationamong these possibilities will require an integrated analysis of both the early and later postseismic geodetic data, with consideration of viscoelastic relaxation (and other) processes within both a composite lower crust and the mantle. It appears likely, in any event, that the early postseismic epoch is shaped by numerous postseismic processes of comparable importance.

4.4. Thin Channel Model

A very different model for the regional viscoelastic relaxation [*Deng et al.*, 1998] possesses a very low-viscosity lower crust (~10^{18} Pa s) and high-viscosity mantle (> ~10^{20} Pa s). It was derived on the basis of the USGS GPS data which included the early (first 3 months) postseismic epoch after the Landers earthquake. *Deng et al.* [1998] included both horizontal and vertical component data and examined a model space consisting of variable elastic plate thickness and lower crustal viscosity. In

support of their viscoelastic model they invoked substantial dip-slip coseismic offsetson the Emerson and Camp Rock faults extending from the surface to ~10 km depth. We can test their viscoelastic model against the larger data set considered here by prescribing a viscoelastic upper crust of the same thickness and viscoelastic lower crust of the same thickness and relaxation time $\tau = \eta_c / \mu_{c2}$ (the actual value of η_c prescribed for this test will differ from the corresponding value in their model simulations because they assumed uniform elastic parameters with depth, in contrast to the layered model of Figure 4), embedded between a purely elastic upper crust and upper mantle. We find that this model, regardless of whether the extra dip-slip components are included or not, yields a serious misfit to the entire southern portion of the observed InSAR image (compare Plate 1a and Plate 4f; this misfit is obscured in the first-order comparison with similar data presented in Figure 1 of *Deng et al.* [1998]) and cannot explain the far-field horizontal velocity patterns.This is reflected in the large χ^2 of InSAR data and far-field GPS data obtained at large η_{m1} and low η_c (Figure 5). The shortcomings of such a high- η_{m1} model have their physical origins in the fact that (1) a thin low-viscosity layer cannot transmit postseismic stresses efficiently into the far field [*Cohen*, 1992; *Pollitz*, 1997] and (2) the vertical postseismic deformation predicted with such a model is invariably positively correlated with the coseismic uplift pattern, precisely the opposite of what is observed (Plates 1a and 4b). The contribution of the horizontal velocity field to the total range change is similar for the low-η_{m1} and high-η_{m1} cases (Plates 4c and 4d). (Large differences between the horizontal velocity vectors for the two cases are, by chance, nearly perpendicular to the range-change azimuth $\hat{\gamma}$, and crustal viscosity for the high-η_{m1} case was chosen to match the observed fault-parallel velocities.) The difference between the low-η_{m1} model and the high-η_{m1} model (Plates 4e and 4f) thus arises from the difference in the predicted vertical postseismic response. Given these differences and the fact that either rapid afterslip or extremely low crustal viscosities ($< \sim 10^{17}$ Pa s) have been deduced from the early postseismic epoch [*Ivins*, 1996; *Yu et al.*, 1996; *Shen et al.*, 1994], we believe that our analysis of the longer-term postseismic relaxation pattern using more data constraints clarifies the regional viscoelastic stratification.

4.5. GPS Uplift Data

We have examined whether available uplift data covering the same 3-year period on the Emerson transect may help distinguish among different candidate viscoelastic models.The observed uplift with respect to a fixed GOLD and corresponding predictions for the Mojave Block model and the high $-\eta_{m1}$ model discussed above are shown in Figure 8. *Savage and Svarc* [1997] suggest that the standard deviation has been underestimated by a factor of 2. The large scatter in the data does not reveal a clear pattern, and signal at the level of the competing viscoelastic models cannot be resolved.

5. Temperature

5.1. Mantle Temperature Inferred From Post-Landers Geodetic Data

Our estimate $8 \pm 4 \times 10^{18}$ Pa s lies within the range of dynamic viscosity 3×10^{18} Pa s to 3×10^{19} Pa s determined by *Zandt and Carrigan* [1993] for the upper mantle under sections of California where conditions for convective instability were apparently satisfied between 5 and 25 Myr ago. One of the competing interpretations of the eastern Mojave Desert mantle discussed in section 5.2 invokes a relatively shallow asthenosphere beneath the region, so that its mechanical similarity with regions of suspected small-scale convection within California may be physically meaningful.

We obtain a first-order estimate of the mantle temperature beneath the central Mojave Domain by considering the Arrhenius relation which represents effective viscosity:

$$\eta_{\text{eff}} = \frac{\sigma}{\dot{\varepsilon}} = \frac{A^{-1}}{\sigma^{n-1}} \exp\left(\frac{Q + PV}{RT}\right). \qquad (12)$$

Here σ and $\dot{\varepsilon}$ are the second invariant of the stress and strain rate tensor, respectively, A is a constant, Q and V are the activation energies for temperature and pressure, respectively, R is the gas constant, and T is the absolute temperature. The parameter $n = 1$ for diffusion creep and $n = 3$ for dislocation creep. The value $n \sim 3.5$ is thought to be appropriate for the continental upper mantle [*Karato and Wu*, 1993]. The parameters A, Q, and V all depend on the material, and η_{eff} further depends on σ. Once these parameters are chosen, (12) provides a direct relation between effective viscosity η_{eff} and temperature T. One property of this relation employed with $n = 3.5$ is that at a given temperature, effective viscosity decreases as σ increases; equivalently, for a given effective viscosity, temperature decreases as σ increases. Two potential contributors to σ in the mantle are the value accumulated during the interseismic interval and the addition of coseismic stress changes from the Landers earthquake itself. The former could be potentially high after the long interseismic period leading up to the Landers event if crust-mantle coupling were assumed to be strong. It cannot be estimated without knowledge of the rheological behavior of the mantle itself, but a reasonable upper bound on it is provided by the stress change at lower crustal depths produced by the Landers coseismic rupture. At a depth of 20 km, σ estimated over the region covered by our geodetic data varies from 0.02 to 3 MPa and averages 0.8 MPa. At uppermost mantle depths (> ~30 km depth), maximum coseismic σ over the region diminshes to 0.57 MPa and continues to diminish rapidly with depth. Therefore a conservative estimate of σ in the subcrust of the central Mojave Domain during the Landers postseismic epoch is 3 MPa. Since a lower bound on T will depend primarily on the upper bound to σ, we adopt this value of σ for use in (12).

From the viscosity value of 8.0×10^{18} Pa s beneath the central Mojave Domain and $\sigma = 3$ MPa, we estimate an uppermost mantle temperature of 1120°C. This temperature is based on the parameters for wet dunite (Fo_{90}) rheology given in Table 2 of *Hirth and Kohlstedt* [1996]. Wet dunite is practically the weakest material that can be used as a proxy for the uppermost mantle, so that temperatures estimated from (12) using its rheology should be minimum estimates. We have neglected the possible effects of pyroxenes and garnet/spinel and iron depletion due to partial melting. *Hirth and Kohlstedt* [1996] summarize studies which suggest that aggregates composed of olivine and

orthopyroxene (the most important secondary mineral) are, in fact, slightly stronger than dunite at a given temperature. An increase in the Mg/Fe ratio such as could be produced by the extraction of basaltic melt would also increase the strength of the material, Fo_{85} being about 15% stronger than Fo_{90} [*Hitchings et al.*, 1989]. Such an iron depletion, even if it could result in a weaker material, would lead to a seismic velocity increase [*Humphreys and Dueker*, 1994], contrary to the low seismic velocities imaged in the central Mojave Domain (Figure 1b). Since Fo_{90} is nearly the pure forsterite end-member of the olivine series, iron enrichment cannot play a significant role in producing the low mantle viscosity. These arguments taken together strongly suggest that the low-viscosity mantle inferred in the central Mojave Domain has a thermal, rather than a compositional, origin.

5.2. Additional Constraints on Sub-Mojave Upper Mantle Temperature

The temperature estimate of 1120˚C is between the wet and dry basalt solidus and is generally consistent with high heat flow [*Sass et al.*, 1994; *Williams*, 1996], the occurrence of Quaternary volcanism [*Wise*, 1969], and low seismic velocities beneath the central/eastern Mojave Domains (Figure 1b). The shallow mantle viscosity range delineated by the data (Figure 6) yields a temperature of 1100–1140˚C. The end-member models discussed in section 4.2 suggest deeper mantle viscosity $\eta_{m2} \leq$ one-third of the shallow mantle viscosity η_{m1}, in which case the deeper upper mantle would be sufficiently high temperature to reach adiabatic conditions. This suggests that convection has shaped the evolution of the sub-Mojave mantle, consistent with the fact that the sub-Mojave mantle has evolved completely from a subcontinental lithosphere to an oceanic mantle geochemical composition from Miocene to Quaternary time [*Musselwhite et al.*, 1989]. This agrees with the fact that temporal geochemical patterns in Miocene to Quaternary basalts in the central Mojave Desert cannot be explained in terms of fractionation of a closed system, but, rather, they reflect sampling of a mantle component similar to that sampled by ocean island basalts [*Glazner et al.*, 1991].

The high uppermost mantle temperature agrees well with low seismic velocity at shallow upper mantle depth (30 to 200+ km depth) in the central Mojave Domain (that is, east of about 117˚W) based on the detailed seismic velocity profile of *Humphreys and Dueker* [1994, Figure 10i]. The mantle portion of this profile is depicted in Figure 1b. This low-velocity pattern also appears in recent tomographic images obtained in the Los Angeles Region Seismic Experiment [*Kohler*, 1999, Figure 5]. Our temperature estimate strongly suggests that the low-velocity region is of thermal rather than compositional origin. The -2.5% velocity differences exhibited here would correspond to a ~200˚C elevation in temperature relative to typical southern California upper mantle. This high temperature is, however, at odds with two independent observations. *Saltus and Thompson* [1995] showed that the elevation difference between the northern and southern Basin and Range can be explained by differences in mantle bouyancy between the two regions, implying a relatively cool uppermost mantle (~800˚C at 40 km depth). This view is consistent with the crustal geotherm derived by

Williams [1996] on the basis of heat flow measurements [*Sass et al.*, 1994] and estimation of radiogenic heat production, which points to a similarly low mantle temperature.

Isotopic compositions from late Cenozoic alkali basalts in the Cima volcanic field in the east central Mojave Desert display a strong affinity with Pacific MORB and late Cenozoic basalts of the California Coast Ranges [*Farmer et al.*, 1995]. From these similarities, *Farmer et al.* [1995] suggest that an upwelling MORB asthenosphere has been present beneath this part of the Mojave Desert for at least the past 8 Myr. Indeed, both the Mojave Desert and Coast Ranges lie at the margin of the Pacific-North America plate boundary which has undergone a transition from a convergent to strike-slip regime during the Neogene [*Atwater and Stock*, 1998]. Northward migration of the Mendocino triple junction is postulated to have resulted in a "slab window" developing in its wake [*Dickinson and Snyder*, 1979; *Lachenbruch and Sass*, 1980]. The existence of a localized upwelling, rather than a broad thermal disturbance such as would be produced by an upwelling mantle plume, may help reconcile the competing interpretations. An upwelling MORB asthenosphere beneath both the east central Mojave Desert and the Coast Ranges is consistent with their similarities in present-day heat flow [*Lachenbruch and Sass*, 1980; *Sass et al.*, 1994]. Owing to its localized nature, the uplift generated by this upwelling is likely less than that generated by a broad thermal disturbance, so it may not conflict with the ~500 m elevation difference between the northern Basin and Range and the east central Mojave Desert. More work is clearly needed to quantitatively verify the conceptual model proposed by *Farmer et al.* [1995]. It appears to be the most promising explanation for the low mantle seismic velocities (Figure 1b), low viscosity (Figure 6), and the additional geodynamic and geochemical constraints discussed above.

5.3. Nature of Possible Thermal Boundary Layer

A possible temperature structure based on the crustal geotherm of *Williams* [1996] and the mantle temperatures inferred here is depicted in Figure 9. This structure is intended as a guide for understanding the many types of geophysical constraints which bear on the state of the sub-Mojave crust and mantle. Since these constraints each carry considerable uncertainties, the structure depicted may be most useful for qualitatively outlining the different temperature domains which exist at various depths.

The suggestion that upwelling asthenosphere exists ~50–70 km depth beneath the east central Mojave Desert raises the possibility of small-scale convection beneath the region. This idea has been explored in the southern Sierra Nevada [*Liu and Shen*, 1998], the Transverse Ranges [*Humphreys and Hager*, 1990; *Jones et al.*, 1996], and elsewhere in California [*Zandt and Carrigan*, 1993]. Our preferred upper mantle temperature structure deduced from the Mojave Block model implies an upper layer from 30 to 50 km depth of "average" temperature 1120˚C underlain by a slightly hotter mantle, though the data considered here cannot resolve the precise nature of the viscosity decrease/temperature increase with depth. If the temperature at the base of the crust is indeed only about 600-700˚C [*Williams*, 1996], then our model can be interpreted in terms of a thermal boundary layer of uncertain thickness (~30 km)

accommodating a 500-600˚C vertical temperature difference. The top few kilometers of the boundary layer may have temperature below 975˚C (Figure 9), and there the material may be quasi-rigid, but below that depth the material behaves viscously with a low average viscosity. The value $\sim 5 \times 10^{18}$ Pa s would represent an effective average viscosity over the boundary layer.

This picture is similar to that described by *Zandt and Carrigan* [1993] for the uppermost mantle which has flowed as upwelling asthenosphere and interacted with the cooler lithosphere, forming a thin thermal boundary layer at that contact. This model has, in turn, been adapted from consideration of Rayleigh instability beneath older oceanic lithosphere [*Parsons and McKenzie*, 1978]. Depending on the Rayleigh number of the mantle flow region, which will depend primarily on the viscosity of the mantle and the temperature difference between the asthenosphere and the cooler lithosphere, this volume of mantle will develop a mature thermal boundary layer, and small-scale convection may be encouraged. If the east central Mojave Desert has reached the conditions for small-scale convection, then we should expect to find a corresponding "downwelling" region. The only candidate downwelling in the region is the high seismic velocity feature beneath the Transverse Ranges imaged by *Humphreys and Hager* [1990] and *Kohler* [1999]. Although they have attributed this feature to convective downwelling of the lithosphere produced by convergence, we suggest that it may be part of a convective system driven by an upwelling asthenosphere beneath the east central Mojave Desert. Alternatively, the viscosity and temperature structure beneath the east central Mojave Desert may be close to, but not satisfy, the conditions for Rayleigh instability.

The presence of a thermal boundary layer within the uppermost mantle is consistent with average lower crust viscosity being about a factor of 2 higher than average uppermost mantle viscosity in our preferred model. Flow parameters for several possible materials which may comprise the lower crust are summarized in Table 3 of *Freed and Lin* [1998]. These parameters lead to a large range of possible mechanical behavior of lower crustal materials depending on several factors, particularly water content. Two representive scales of crustal viscosity as a function of temperature are included in Figure 9 using wet and dry Westerly granite. Figure 14 of *Freed and Lin* [1998] shows that most other crustal materials are intermediate between these two. Lower crustal temperatures prescribed by the *Williams* [1996] geotherm appear adequate to explain the lower crustal viscosity of 1.6×10^{19} Pa s obtained in the Mojave Block model with $\eta_c / \eta_{m1} = 2$, provided that a hydrous crustal rheology is chosen. Without a strong thermal boundary layer the estimated viscosity of the lower crust could be obtained with a dry rheology and higher temperatures ~900˚C, but this would compromise the geotherm of *Williams* [1996]. There are many factors which should be considered in such an evaluation, such as uncertainty related to the extrapolation of surface heat flow to depth, the assumption of dislocation creep, the appropriate differential stress, the extrapolation of laboratory data to low geologic strain rates, and the effects of grain size, melt fraction, and interconnectedness of the weakest consituent of a biviscous lower crust [*Ivins and Sammis*, 1996]. The relative importance of these factors may be better established with more detailed examination of the early and late post-Landers deformation

process.

6. Geologic Implications

On the basis of the likely thermal origin of the low viscosity and seismic velocity of the uppermost mantle beneath the central Mojave Domain, we suggest that the existence, location, and width of the ECSZ are genetically related to the weakness of the upper mantle beneath it. We arrive at this proposition by considering the variations in mantle strength across the region together with the distribution of crustal faulting. Figure 1b shows that the mantle beneath the east central Mojave Domain possesses low velocity, whereas that beneath the western Mojave Domain possesses very high velocity. The viscosity structure derived in this paper together with the geochemical evidence strongly suggests a thermal origin for the low seismic velocity region. It is likely that the high seismic velocities beneath the western Mojave Domain, particularly the southwestern portion, can be attributed to a correspondingly low mantle temperature. They have been interpreted as a convective downwelling of subcrustal lithosphere beneath the Transverse Ranges [*Humphreys and Hager*, 1990; *Kohler*, 1999]. From the relation between strength and temperature (equation (12)) it follows that mechanically weak and strong mantle must be present beneath the east central and western Mojave Domains, respectively. If we extrapolate current mechanical behavior to the time when late Cenozoic heating began affecting the region (26-18 Ma) [*Dokka*, 1986], then since this heat input the mantle beneath the east central Mojave Domain has been thermally weakened and caught in a newly formed dextral shear zone (the San Andreas fault system) bounded to the west by the stronger western Mojave Domain. It appears that these attributes of the Mojave Desert region are fundamentally responsible for (1) the pervasive dextral faulting and block rotation which have shaped the east central Mojave Domain region since middle to late Miocene time [*Dokka and Travis*, 1990] and continue to the present day [*Sauber et al.*, 1994] and (2) the almost total absence of active faults beneath the western Mojave Domain [*Unruh et al.*, 1994].

Our results thus lend credibility to the idea proposed by *Kusznir* [1982] that much of the western United States consists of a thin horizontal stress guide; that is, it has been sufficiently thermally weakened that the upper lithosphere is effectively thin and subject to large amplications of externally applied stresses, making it a locus of large scale faulting. The ECSZ represents the natural boundary between the southern Great Basin, which possesses a weak uppermost mantle and the western Mojave Domain/San Gabriel Block, which possesses a strong uppermost mantle.

This association between the distribution of active surface faults and the strength of the mantle may be applicable to other regions as well. For example, the northern Coast Ranges, California, are underlain by warm uppermost mantle material [e.g., *Benz et al.*, 1992] and contain a denser network of faults than the surrounding California lithosphere. The continuation of the ECSZ farther north of the Garlock fault may be related to the presence of warm, buoyant material beneath the southern Sierra Nevada that continues eastward into the southern Great Basin [e.g., *Wernicke et al.*, 1996; *Pollitz*, 1999], in contrast to the

unfaulted nature of most of the Sierra Nevada block which is underlain by relatively high-velocity (and presumably low temperature) material at uppermost mantle depths [*Benz et al.* , 1992; *Humphreys and Dueker*, 1994; *Pollitz*, 1999].

7. Conclusions

We have analyzed a combination of GPS and InSAR data collected during the 3.5 years following the 1992 Landers earthquake in the central Mojave Domain. The GPS data set covers near-, intermediate-, and far-field distances away from the Landers rupture zones and provides a discrete (but nevertheless fairly dense) sample of the horizontal postseismic velocity field. The InSAR data set covers near- and intermediate-field distances and adds essentially spatially continous coverage of the vertical postseismic velocity field.The interseismic velocity field is dwarfed by the observed postseismic velocity field, so that the observed velocity field must be the product of processes which are unique to the Landers postseismic epoch. The combination of GPS and InSAR that we have considered allows us to discriminate, first, among competing postseismic processes, particularly afterslip versus deep viscoelasticrelaxation driven by the coseismic stress changes; and second, to discriminate among possible models of deep viscoelastic relaxation.

Once we establish the importance of deep viscoelastic relaxation, our study examines essentially a two-dimensional model space consisting of crust and mantle viscosity. We find that the shallow mantle viscosity beneath the central Mojave Domain is low ($8 \pm 4 \times 10^{18}$ Pa s) in agreement with independent inferences of a warm regional uppermost mantle. The deeper (>50 km) upper mantle viscosity is estimated at 2.7×10^{18} Pa s in our preferred model. Although the inferences we can draw about the deeper viscosity are limited, the end-member models discussed in section 4.1 suggest that the broadest range of deeper upper mantle viscosity consistent with the geodetic data is about $1-6 \times 10^{18}$ Pa s. This is in the range expected for young oceanic mantle below the dehydration boundary [*Hirth and Kohlstedt*, 1996], in agreement with the inference of an asthenosphere no deeper than 50–70 km based on isotopic compositions of late Cenozoic alkali basalts [*Livaccari and Perry*, 1993]. This is further consistent with the interpretation of a slab window having developed beneath this part of the Mojave Desert following the transition from a convergent to a strike-slip plate boundary during the Neogene [*Farmer et al.*, 1995].

Slow seismic velocities beneath the eastern Mojave Domain are likely thermally induced. If seismic velocity variations between the western and eastern Mojave Domain are also attributed to temperature, then this implies correspondingly large variations in uppermost mantle strength. In that case, there is a strong correlation between uppermost mantle strength and the distribution of surface faults within the Mojave Block, the east central Mojave Domain being permeated with numerous faults that form the ECSZ and the western Mojave Domain being nearly devoid of faults.

Our inference that mantle relaxation explains most of the long-wavelength post-Landers transient velocity field carries additional implications. First, at similar temperature, crustal materials should be weaker than mantle materials. Although a

composite crustal rheology with polymineralic rock types is complicated to assess, a weaker mantle may imply a strong thermal boundary layer within the shallow mantle. Heat flow data around the Landers rupture zone imply a lower crustal temperature no greater than ~700°C, which is consistent with available geodetic estimates of lower crustal viscosity for most wet rheologies. A dry lower crust combined with a much weaker temperature gradient in the uppermost mantle could explain available crust and mantle viscosity estimates only if lower crustal temperature were far greater than heat flow data suggest. Clarification of the state of the lower crust must await more a detailed integrated study of the early and late postseismic epochs, with focus on the mechanical behavior of a biviscous lower crust. Second, a weak mantle encourages small-scale convection, which may have a substantial effect on crustal stresses. This idea has been previously explored throughout California (e.g., southern Sierra Nevada, northern Coast Ranges, Transverse Ranges, the Southern Great Valley seismic "anomaly"), and it may also play a role in localization of faulting in this part of the ECSZ.

Acknowledgments. This work was supported by the Cooperative UC/Los Alamos Research program and the IGPP program of Lawrence Livermore National Laboratory. We thank Yehuda Bock, Jishu Deng, Liz Hearn, Barry Parsons, and Jim Savage for helpful discussions. We thank Zheng-Kang Shen and Jerry Svarc for helping us acquire the SCEC and USGS GPS data, respectively; Evelyn Price for scrutinizing a preliminary draft; and Jean Chery, Ruth Harris, and Liz Hearn for their incisive reviews.

References

Abramowitz, M., and I.A. Stegun, *Pocketbook of Mathematical Functions With Formulas, Graphs, and Mathematical Tables*, 468 pp., Natl. Inst. of Stand. and Technol., Gaithersburg, Md., 1984.

Atwater, T., and J. Stock, Pacific-North America plate tectonics of the Neogene southwestern United States: An update, *Int. Geol. Rev., 40*, 375-402, 1998.

Basaltic Volcanism Study Project, Experimental petrology of basalts and their source rocks, in *Basaltic Volcanism in the Terrestrial Planets*, pp. 493-630, Pergamon, Tarrytown, N.Y., 1981.

Behr, J., R. Bilham, P. Bodin, and S. Gross, Eureka Peak Fault afterslip following the 28 June 1992 Landers earthquake, *Bull. Seismol. Soc. Am., 84*, 826-834, 1994.

Benz, H.M., G. Zandt, and D.H. Oppenheimer, Lithospheric structure of northern California from teleseismic images of the upper mantle, *J. Geophys. Res., 97*, 4791-4807, 1992.

Bott, N.H.P., and D.S. Dean, Stress diffusion from plate boundaries, *Nature, 243*, 339-341, 1973.

Brace, W.F. and D.L. Kohlstedt, Limits of lithospheric stress imposed by laboratory experiments, *J. Geophys. Res., 85* , 6348-6252, 1980.

Brocher, T.M., J. McCarthy, P.E. Hart, W.S. Holbrook, K.P. Furlong, T.V. McEvilly, J.A. Hole, and S.L. Klemperer, Seismic evidence for a lower-crustal detachment beneath San Francisco Bay, California, *Science, 265*, 1436-1439, 1994.

Buck, W.R., Modes of continental lithospheric extension, *J. Geophys. Res., 96*, 20,161-20,178, 1991.

Chen, W.-P., and P. Molnar, Focal depths of intracontinental and intraplate earthquakes and their implications for the

thermal and mechanical properties of the lithosphere, *J. Geophys. Res., 88*, 4183-4214, 1983.

Chery, J., J. P. Vilotte, and M. Daignieres, Thermomechanical evolution of a thinned continental lithosphere under compression; implications for the Pyrenees, *J. Geophys. Res., 96* , 4385-4412, 1991.

Cohen, S.C., A multilayer model of time dependent deformation following an earthquake on a strike slip fault, *J. Geophys. Res., 87*, 5409-5421, 1982.

Cohen, S.C., Postseismic deformation and stress diffusion due to viscoelasticityand comments on the modified Elsasser model, *J. Geophys. Res., 97*, 15,395-15,403, 1992.

Deng, J., M. Gurnis, H. Kanamori, and E. Hauksson, Viscoelastic flow in the lower crust after the 1992 Landers, California, earthquake, *Science, 282*, 1689-1692, 1998.

Dickinson, W.R., and W.S. Snyder, Geometry of subducted slabs related to San Andreas transform, *J. Geol., 87*, 609-627, 1979.

Dokka, R.K., Patterns and modes of early Miocene crustal extension, central MojaveDesert, California, *Spec. Pap. Geol. Soc. Am., 208*, 75-95, 1986.

Dokka, R.K., and C.J. Travis, Late Cenozoic strike-slip faulting in the Mojave Desert, California, *Tectonics, 9*, 311-340, 1990.

Donnellan, A., and G.A. Lyzenga, GPS observations of fault afterslip andupper crustal deformation following the Northridge earthquake, *J. Geophys. Res., 103*, 21285-21297, 1998.

European Space Agency, ERS-1 System, 87 pp., ESA Publ. Div., Eur. Space Res. and Technol. Cent., Noordwijk, Netherlands, 1992.

Farmer, G.L., A.F. Glazner, H.G. Wilshire, J.L. Wooden, and W.J. Pickthorn, Origin of late Cenozoic basalts at the Cima volcanic field, Mojave Desert, California, *J. Geophys. Res., 100*, 8399-8415, 1995.

Feigl, K.L., et al., Space geodetic measurement of crustal deformation in central and southern California, 1984-1992, *J. Geophys. Res., 98*, 21,677-21,712, 1993.

Freed, A.M., and J. Lin, Time-dependent changes in failure stress following thrust earthquakes, *J. Geophys. Res., 103* , 24,393-24,409, 1998.

Furlong, K.P., W.D. Hugo, and G. Zandt, Geometry and evolution of the San Andreas fault in northern California, *J. Geophys. Res., 94*, 3100-3110, 1989.

Glazner, A.F., G.L. Farmer, W.T. Hughes, J.L. Wooden, and W. Pickthorn, Contamination of basaltic magma by mafic crust at Amboy and Pisgah craters, Mojave Desert, California, *J. Geophys. Res., 96*, 13,673-13,691, 1991.

Hacker, B.R., A. Yin, J. M. Christie, and G. A. Davis, Stress magnitude, strain rate and rheology of extended middle continental crust inferred from quartz grain sizes in the Whipple Mountains, California, *Tectonics, 11*, 36-46, 1992.

Hart, E.W., W.A. Bryant, and J.A. Treiman, Surface faulting associated with the June 1992 Landers earthquake, California, *Geology, 46*, 10-16, 1993.

Hauksson, E., L.M. Jones, K. Hutton, and D. Eberhart-Phillips, The 1992 Landers earthquake sequence: Seismological observations, *J. Geophys. Res., 98*, 19,835-19,858, 1993.

Hirth, G., and D.L. Kohlstedt, Water in the oceanic upper mantle: Implicationsfor rheology, melt extraction and the evolution of the lithosphere, *Earth Planet. Sci. Lett., 144*, 93-108, 1996.

Hitchings, R.S., M.S. Paterson, and J. Bitmead, Effects of iron and magnetite additions in olivine-pyroxene rheology, *Phys. Earth Planet. Inter., 55*, 277-291, 1989.

Humphreys, E.D., and K.G. Dueker, Western U.S. upper mantle structure, *J. Geophys. Res., 99*, 9615-9634, 1994.

Humphreys, E.D., and B.H. Hager, A kinematic model for the late Cenozoic development of southern California crust and upper mantle, *J. Geophys. Res., 95*, 19,747-19,762, 1990.

Ivins, E.R., Transient creep of a composite lower crust, 2, A polymineralic basis for rapidly evolving postseismic deformation modes, *J. Geophys. Res., 101*, 28,005-28,028, 1996.

Ivins, E.R., and C.G. Sammis, Transient creep of a composite lower crust, 1, Constitutive theory, *J. Geophys. Res., 101*, 27,981-28,004, 1996.

Jones, C.H., J.R. Unruh, and L.J. Sonder, The role of gravitational potential energy in active deformation in the southwestern United States, *Nature, 381*, 37-41, 1996.

Jones, L.E., and D.V. Helmberger, Source parameters of the 1992 Big Bear sequence, *Eos Trans. AGU, 74* (16), Spring Meet. Suppl., 215, 1993.

Karato, S.-I., and P. Wu, Rheology of the upper mantle: A synthesis, *Science, 260,* 771-778, 1993.

Karato, S.-I., D. C. Rubie, and H. Yan, Dislocation recovery in olivine under deep upper mantle conditions; implications for creep and diffusion, *J. Geophys. Res., 98*, 9761-9768, 1993.

Kay, R. W., and S. M. Kay, The nature of the lower continental crust: Inferences from geophysics, surface geology, and crustal xenoliths, *Rev. Geophys., 19*, 271-297, 1981.

Kohler, M.D., Lithospheric deformation beneath the San Gabriel Mountains in the southern California Transverse Ranges, *J. Geophys. Res., 104*, 15,025-15,041, 1999.

Kusznir, N.J., Lithosphere response to externally and internally derived stresses: A viscoelastic stress guide with amplification, *Geophys. J. R. Astron. Soc., 70* , 399-414, 1982.

Kusznir, N.J., The distribution of stress with depth in the lithosphere; thermorheological and geodynamic constraints, *Philos. Trans. R. Soc. London, Ser. A, 337*, 95-110, 1991.

Lachenbruch, A.H., and J.H. Sass, Heat flow and energetics of the San Andreas fault zone, *J. Geophys. Res., 85*, 6185-6222, 1980.

Lithgow-Bertelloni, C., and P.G. Silver, Dynamic topography, plate driving forces and the African superswell, *Nature, 395*, 269-272, 1998.

Liu, M., and Y. Shen, Sierra Nevada uplift: A ductile flank to mantle upwelling under the Basin and Range province, *Geology, 26*, 299-302, 1998.

Livaccari, R.F., and F.V. Perry, Isotopic evidence for preservation of Cordilleran lithospheric mantle during the Sevier-Laramide orogeny, western United States, *Geology, 21*, 719-722, 1993.

Massonnet, D., K. Feigl, M. Rossi, and F. Adragna, Radar interferometric mapping of deformation in the year after the Landers earthquake, *Nature, 369*, 227-230, 1994.

Massonnet, D., W. Thatcher, and H. Vadon, Detection of postseismic fault-zone collapse following the Landers earthquake, *Nature, 382*, 612-616, 1996.

Miyashita, K., A model of plate convergence in southwest Japan, inferred from leveling data associated with the 1946 Nankaido earthquake, *J. Phys. Earth, 35*, 449-467, 1987.

Molnar, P., and P. Tapponier, A possible dependence of tectonic strength on the age of the crust in Asia, *Earth Planet. Sci. Lett., 52*, 107-114, 1981.

Musselwhite, D. S., D. J. DePaolo, and M. McCurry, The evolution of a silicic magma system: Isotopic and chemical evidence from the Woods Mountains Volcanic Center, eastern California, *Contrib. Mineral.Petrol., 101*, 19-29, 1989.

Nur, A., and G. Mavko, Postseismic viscoelastic rebound,

Science, 183, 204-206, 1974.

Okada, Y., Surface deformation due to shear and tensile faults in a half-space, *Bull. Seismol. Soc. Am., 75* , 1135-1154, 1985.

Parsons, B., and D.P. McKenzie, Mantle convection and the thermal structure of the plates, *J. Geophys. Res., 83*, 4485-4496, 1978.

Peltzer, G., P. Rosen, F. Rogez, and K. Hudnut, Postseismic rebound in fault step-overs caused by pore fluid flow, *Science, 273*, 1202-1204, 1996.

Peltzer, G., P. Rosen, F. Rogez, and K. Hudnut, Poro-elastic rebound along the Landers 1992 earthquake surface rupture, *J. Geophys. Res., 103*, 30,131-30,145, 1998.

Pollitz, F.F., Gravitational-viscoelastic postseismic relaxation on a layered spherical Earth, *J. Geophys., Res., 102* , 17,921-17,941, 1997.

Pollitz, F.F., Regional velocity structure in northern California from inversion of scattered seismic surface waves, *J. Geophys. Res., 104*, 15,043-15,072, 1999.

Pollitz, F.F., and I.S. Sacks, Modeling of postseismic relaxation following the Great 1857 earthquake, southern California, *Bull. Seismol. Soc. Am., 82*, 454-480, 1992.

Pollitz, F.F., and I.S. Sacks, Fault model of the 1891 Nobi earthquake from historic triangulation and levelling, *J. Phys. Earth, 42*, 1-43, 1994.

Pollitz, F.F. and I.S. Sacks, Viscosity structure beneath northeast Iceland, *J. Geophys. Res., 101* , 17,771-17,793, 1996.

Pollitz, F.F., R. Bürgmann, and P. Segall, Joint estimation of afterslip rate and postseismic relaxation following the 1989 Loma Prieta earthquake, *J. Geophys. Res., 103* , 26,975-26,992, 1998.

Qu, J., T.L. Teng, and J. Wang, Modeling of short-period surface-wave propagation in southern California, *Bull. Seismol. Soc. Am., 84*, 596-612, 1994.

Rydelek, P.A., and I.S. Sacks, Asthenospheric viscosity and stress diffusion: A mechanism to explain correlated earthquakes and surface deformations in northeast Japan, *Geophys. J. Int., 100*, 39-58, 1990.

Saltus, R.W., and G.A. Thompson, Why is it downhill from Tonopah to Las Vegas? A case for mantle support of the high northern Basin and Range, *Tectonics, 14*, 1235-1244, 1995.

Sass, J.H., et al., Thermal regime of the southern Basin and Range province, 1, Heat flow data from Arizona and the Mojave Desert of California and Nevada, *J. Geophys. Res., 99*, 22,093-22,119, 1994.

Sauber, J., W. Thatcher, S.C. Solomon, and M. Lisowski, Geodetic slip rate for the Eastern California Shear Zone and the recurrence time of Mojave Desert earthquakes, *Nature, 367*, 264-266, 1994.

Savage, J.C., Equivalent strike-slip earthquake cycles in half-space and lithosphere-asthenosphere Earth models, *J. Geophys. Res., 95*, 4873-4879, 1990.

Savage, J.C., and J.L. Svarc, Postseismic deformation associated with the 1992 M_w = 7.3 Landers earthquake, southern California, *J. Geophys. Res., 102*, 7565-7577, 1997.

Shen, Z.-K., et al., Postseismic deformation following the Landers earthquake, California, 28 June 1992, *Bull. Seismol. Soc. Am., 84*, 780-791, 1994.

Sibson, R.H., Fault zone models, heat flow, and the depth distribution of earthquakes in the continental crust of the United States, *Bull. Seismol. Soc. Am., 72*, 151-163, 1982.

Sieh, K., et al., Near-field investigations of the Landers earthquake sequence, April to July 1992, *Science, 260*, 171-176,

1993.
Stewart, J.H., Basin-range structure in western North America: A review, *Mem. Geol. Soc. Am., 152*, 1-31, 1978.
Tabei, T., Crustal movements in the inner zone of southwest Japan associated with stress relaxation after major earthquakes, *J. Phys. Earth, 37*, 101-131, 1989.
Thatcher, W., T. Matsuda, T. Kato, and J.B. Rundle, Lithospheric loading by the 1896 Riku –u earthquake, northern Japan: Implications for plate flexure and asthenospheric rheology, *J. Geophys. Res., 85*, 6429-6435, 1980.
Unruh, J., W. R. Lettis, and J. M. Sowers, Kinematic interpretation of the 1992 Landers earthquake, *Bull. Seismol. Soc. Am., 84*, 537-546, 1994.
Wald, D.J., and T. H. Heaton, Spatial and temporal distribution of slip for the 1992 Landers, California, earthquake, *Bull. Seismol. Soc. Am., 84*, 668-691, 1994.
Wdowinski, S., and Y. Bock, The evolution of deformation and topography of high elevated plateaus, 2, Application to the central Andes, *J. Geophys. Res., 99*, 7121-7130, 1994.
Wdowinski, S., Y. Bock, J. Zhang, P. Fang, and J. Genrich, Southern California Permanent GPS Geodetic Array: Spatial filtering of daily position for estimating coseismic and postseismic displacement induced by the 1992 Landers earthquake, *J. Geophys. Res., 102*, 18,057-18,070, 1997.
Wernicke, B., et al., Origin of high mountains on continents: The southern Sierra Nevada, *Science, 271*, 190-193, 1996.
Williams, C.F., Temperature and the seismic/aseismic transition: Observations from the 1992 Landers earthquake, *Geophys. Res. Lett., 23*, 2029-2032, 1996.
Wise, W., Origin of basaltic magmas in the Mojave Desert area, California, *Contrib. Mineral. Petrol., 23*, 53-64, 1969.
Yu, T.-T., J.B. Rundle, and J. Fernandez, Surface deformation due to a strike-slip fault in an elastic gravitational layer overlying a viscoelastic gravitational half-space, *J. Geophys. Res., 101*, 3199-3214, 1996. (Correction to "Surface deformation due to a strike-slip fault in an elastic gravitational layer overlying a viscoelastic gravitational half-space", *J. Geophys. Res., 104*, 15,313-15,315, 1999.)
Zandt, G., and C.R. Carrigan, Convective instability and upper mantle viscosity under California, *Science, 261*, 460-463, 1993.
Zeyen, H., et al., Styles of continental rifting: Crust-mantle detachment and mantle plumes, *Tectonophysics, 278*, 329-352, 1997.

R Bürgmann, Department of Geology and Geophysics, University of California, Berkeley, CA 94720.

G. Peltzer, Jet Propulsion Laboratory, MS 183-501, 4800 Oak Drive, Pasadena, CA 91109

F. F. Pollitz, Department of Geology, 1 Shields Ave. University of California, Davis, CA 95616. (pollitz@geology.ucdavis.edu)

(Received May 13, 1999; revised September 27, 1999;
accepted October 21, 1999.)

Copyright 2000 by the American Geophysical Union.

Paper number 1999JB900380

Figure 1. (a) Active faults around the Mojave Desert region. Boxed region indicates the area covered in Figure 2 and Plates 1a, 1b, 2, 3a, 3c, and 4. (b) P-wave velocity anomalies in percent of background velocity [*Humphreys and Dueker*, 1994, Figure 10i] across the profile indicated in Figure 1a. The low seismic velocity pattern underlying this portion of the central Mojave Domain at uppermost mantle depths continues northwestward to include essentially all of the central Mojave Domain [e.g., *Humphreys and Dueker*, 1994, Figure 9].

Figure 2. Map of the June 28, 1992, Landers earthquake area. Solid lines are the June 28, 1992, surface rupture [*Sieh et al.*, 1993]. Shade depicts topography from U.S. Geological Survey (USGS) digital elevation model. White dots are aftershocks between August 7, 1992, and January 23, 1996 [*Hauksson et al.*, 1993]. After *Peltzer et al.* [1998].

Figure 3. (a) Bold lines are the surface projection of buried fault planes used by *Feigl et al.* [1993] and *Savage and Svarc* [1997] to represent interseismic strain accumulation in southern California. Dashed lines represent active faults in California. (b) Interseismic velocity field evaluated at 26 GPS sites used in this study relative to a fixed Goldstone.

Figure 4. Viscoelastic stratification used to model postseismic deformation in the Landers epicentral area. A purely elastic upper crust (base at 16 km depth) is underlain by a standard linear solid lower crust [*Cohen*, 1982] (base at 30 km depth) and Maxwell viscoelastic fluid upper mantle. Parameters κ, μ, and η are the bulk modulus, shear modulus, and viscosity, respectively, and μ' is the long-term strength of the lower crust ($\mu' = 0$ would correspond to a Maxwell viscoelastic fluid). Elastic stratification is prescribed by values $\kappa_{c1} = 74$ GPa, $\mu_{c1} = 41$ GPa, $\kappa_{c2} = 95$ GPa, $\mu_{c2} = 53$ GPa, and $\kappa_m = 150$ GPa, $\mu_m = 70$ GPa. An additional elastic layer from 0 to 4 km depth (not shown) is prescribed with $\kappa = 65$ GPa and $\mu = 36$ GPa. This stratification is essentially (with fewer discontinuities) equivalent to the seismic structure for the eastern Mojave Desert given in Table 1 of *Qu et al.* [1994]. Parameters η_c, η_{m1}, η_{m2}, and μ' are variable.

Figure 5. (left) Misfit with respect to several data subsets in $\eta_{m1} - \eta_c / \eta_{m1}$ space for $\mu' = 12$ GPa and $\eta_{m1} / \eta_{m2} = 3$. (right) Corresponding misfit pattern for the case $\mu' = 0$ (Maxwell viscoelastic fluid lower crust). Dashed lines indicate lowest two contours associated with each subset. The Mojave Block model is indicated by the solid circles in Figure 5 (left).

Figure 6. Ω_F (defined in section 3.2) at probability levels $P = 0.95$ and $P = 0.99$ through the model slices $\mu' = 12$ GPa and $\mu' = 0$, for $\eta_{m1} / \eta_{m2} = 3$.

Figure 7a. Misfit with respect to several data subsets in $\eta_{m1} - \eta_c / \eta_{m1}$ space for $\mu' = 12$ GPa and $\eta_{m1} / \eta_{m2} = 1$. The best isoviscous mantle model is indicated by the solid circles.

Figure 7b. Ω_F (defined in section 3.2) at probability levels $P = 0.95$ and $P = 0.99$ through the model slice $\mu' = 12$ GPa, for the isoviscous mantle model.

Figure 8. Observed uplift with respect to GOLD and corresponding calculated uplift on the Mojave Block model and the high-η_{m1} model discussed in the text at the 10 GPS sites on the Emerson transect (Plates 4a and 4b). Error bars denote $\pm$standard deviation in measurement.

Figure 9. Possible temperature structure beneath the east central Mojave Desert based on the crustal geotherm of *Williams* [1996], the mantle temperature structure implied by the Mojave Block model (section 5.1), and geochemical evidence for a shallow asthenosphere. Two crustal geotherms of *Williams* [1996] correspond to the range of heat flow values observed in the Landers region. A thermal boundary layer between 30 and 60 km depth is envisioned to accommodate a 500-600˚C vertical temperature difference at the top of the mantle. The thin subcrustal domain at temperature below 975˚C may exhibit quasi-rigid behavior, but the upper 30 km of the mantle as a whole has an average temperature consistent with a viscosity of $\sim 5 \times 10^{18}$ Pa s. An adiabatic temperature gradient of 0.5˚C/km is assumed for the temperature in the asthenosphere below 60 km. Ranges of sub-Mojave mantle viscosity from depth 30-50 km (η_{m1}) and >50 km (η_{m2}) determined in this study are indicated. The dry and wet peridotite solidus are from *Basaltic Volcanism Study Project* [1981]. Viscosity of the mantle and crust as a function of temperature are indicated by the upper tick lines. They are calculated from equation (12) with flow parameters of wet dunite [*Hirth and Kohnstedt*, 1996], and wet and dry Westerly granite [*Freed and Lin*, 1998, Table 3], respectively, assuming 3 MPa differential stress. The pressure dependence is included only for the mantle viscosity calculation.

Plate 1. (a) Observed range change from September 1992 to January 1996 [*Peltzer et al.*, 1998]. (b) Calculated range change (equation (4)) on Mojave Block model (see section 3.2). (c) Observed average horizontal velocity with respect to fixed Goldstone from November 1992 to December 1995 and corresponding 1 σ error ellipses [*Savage and Svarc*, 1997; Southern California Earthquake Center (SCEC) Release 2, 1998, available at http://www.scecdc.scec.org/group_e/ release.v2]. Calculated horizontal velocity vectors (equation (3)) on Mojave Block model are shown as black arrows. The seven SCEC GPS sites lying outside of the boxed region are

referred to as "far field"; all remaining GPS sites are considered "near field" (Table 1).

Plate 2. Surface displacement predicted by (a) *Savage and Svarc* [1997] afterslip model, (b) poroelastic model, and (c) the combination of Plates 2a and 2b. One color cycle represents 5.6 cm of surface displacement towards the radar. Black arrows depict horizontal displacement vectors. White lines show fault geometry of *Savage and Svarc* [1997] afterslip model (Plate 2a) and of *Wald and Heaton's* [1994] coseismic model (Plates 2b and 2c). After *Peltzer et al.* [1998].

Plate 3. (a) Calculated range change and (b) horizontal displacements on a model with an isoviscous mantle: $\eta_{m1} = \eta_{m2} = 6.0 \times 10^{18}$ Pa s, $\eta_c / \eta_{m1} = 2.0$, $\mu' = 12$ GPa. (c and d): Corrsponding calculated range change and horizontal displacement field on a model with a factor of 10 contrast in mantle viscosity at 50 km depth: $\eta_{m1} = 1.1 \times 10^{19}$ Pa s, $\eta_{m1} = 1.1 \times 10^{18}$ Pa s, $\eta_c / \eta_{m1} = 2.0$, $\mu' = 12$ GPa. Superimposed in Plates 3b and 3d are the observed horizontal velocity vectors from Figure 1c.

Plate 4. (a) Range change contributed from vertical postseismic velocity field on the Mojave Block model. (b) Corresponding range change on a thin channel model parameterized by $\eta_c = 5 \times 10^{18}$ Pa s, $\eta_{m1} = \eta_{m2} = \infty$, and $\mu' = 0$ (η_c chosen to duplicate observed near-field fault-parallel postseismic velocities). The pattern in Plate 4a is negatively correlated with the coseismic uplift pattern and positively correlated with the observed postseismic range change (Plate 1a), whereas the pattern in Plate 4b is positively correlated with the coseismic uplift pattern and negatively correlated with the observed postseismic range change. (c and d) Range change contributed from horizontal postseismic velocity field on the Mojave Block and thin channel models, respectively. (e and f) Total range change patterns, equal to the sum of Plates 4a and 4c or Plates 4b and 4d, respectively. In Plates 4a and 4b, lighter dashed lines and triangles denote the USGS sites on the Emerson transect.

Table 1. GPS Sites and Horizontal Velocities

Site	Lat N	Lon E	v_e, [a] mm/yr	v_n, [a] mm/yr	v_I, [b] mm/yr	□ [b]	Type [c]	Source
PIN1	33.612	-116.458	-6.15	13.55	16.91	-59.61	N	USGS
GOLD	35.425	-116.889	0.00	0.00	0.00	0.00	(Æxed)	USGS
SANH	34.255	-116.278	10.86	-2.52	2.26	-117.47	N	USGS
LAW1	34.542	-116.588	-0.94	2.67	0.88	-89.12	N	USGS
LAW2	34.526	-116.623	-6.06	10.59	1.01	-81.86	N	USGS
LAW3	34.501	-116.669	-1.68	7.65	1.24	-74.67	N	USGS
LAW4	34.453	-116.665	-3.79	13.40	1.47	-74.33	N	USGS
LAE1	34.574	-116.557	-7.56	0.92	0.75	-97.59	N	USGS
LAE2	34.588	-116.522	-4.21	-0.93	0.70	-106.71	N	USGS
LAE3	34.617	-116.486	5.50	-4.63	0.64	-117.23	N	USGS
LAE4	34.734	-116.329	1.50	-6.43	0.67	-149.01	N	USGS
OLDD	34.390	-116.697	-1.65	13.16	2.03	-70.39	N	USGS
OLDW	34.388	-116.751	-2.92	11.46	2.33	-66.48	N	USGS
6052	34.515	-116.840	-10.09	7.31	1.84	-63.65	N	SCEC
7000	34.676	-116.715	-9.65	1.39	0.71	-75.88	N	SCEC
7001	34.560	-116.469	-1.37	-9.31	0.79	-115.81	N	SCEC
BALD	34.462	-117.393	-10.85	8.31	5.95	-69.02	F	SCEC
BEAR	34.264	-116.884	-7.85	19.63	5.03	-63.82	N	SCEC
HECT	34.784	-116.420	0.11	-8.72	0.49	-146.37	N	SCEC
HODG	34.833	-117.170	-7.43	6.02	0.96	-71.12	F	SCEC
JUNI	34.401	-117.183	-16.04	14.97	5.33	-66.13	F	SCEC
LAZY	34.343	-116.513	3.32	10.82	1.72	-95.15	N	SCEC
MOOD	34.608	-117.688	-5.28	7.30	5.68	-58.08	F	SCEC
ONYX	34.192	-116.709	-0.18	16.13	4.68	-68.74	N	SCEC
POIN	34.453	-117.067	-8.08	10.01	3.65	-64.33	F	SCEC
SOAP	34.903	-116.980	-3.26	3.14	0.42	-76.70	F	SCEC
SUNH	34.749	-117.297	-6.72	8.00	1.72	-69.77	F	SCEC

[a] v_e and v_n are east and north velocity, respectively.

[b] v_I and □ are interseismic velocity and azimuth (degrees clockwise from due north)

[c] N, near-Æeld site; F, far-Æeld site.

Figure 1

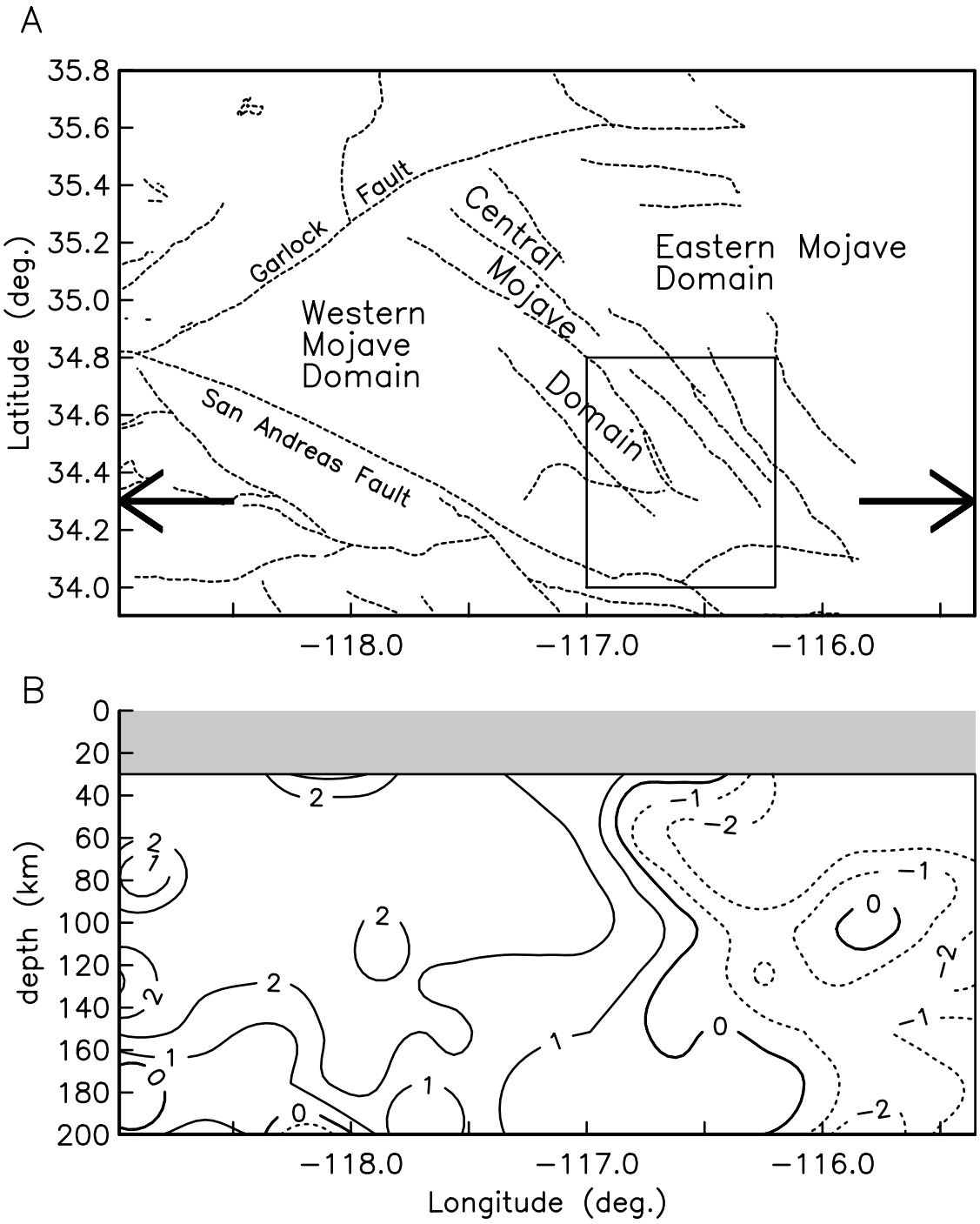
A
35.8
35.6
35.4
35.2
35.0
34.8
34.6
34.4
34.2
34.0
Latitude (deg.)
Garlock Fault
Central Mojave Domain
Eastern Mojave Domain
Western Mojave Domain
San Andreas Fault
−118.0
−117.0
−116.0
B
0
20
40
60
80
100
120
140
160
180
200
depth (km)
2
1
0
−1
−2
−118.0
−117.0
−116.0
Longitude (deg.)

Figure 2

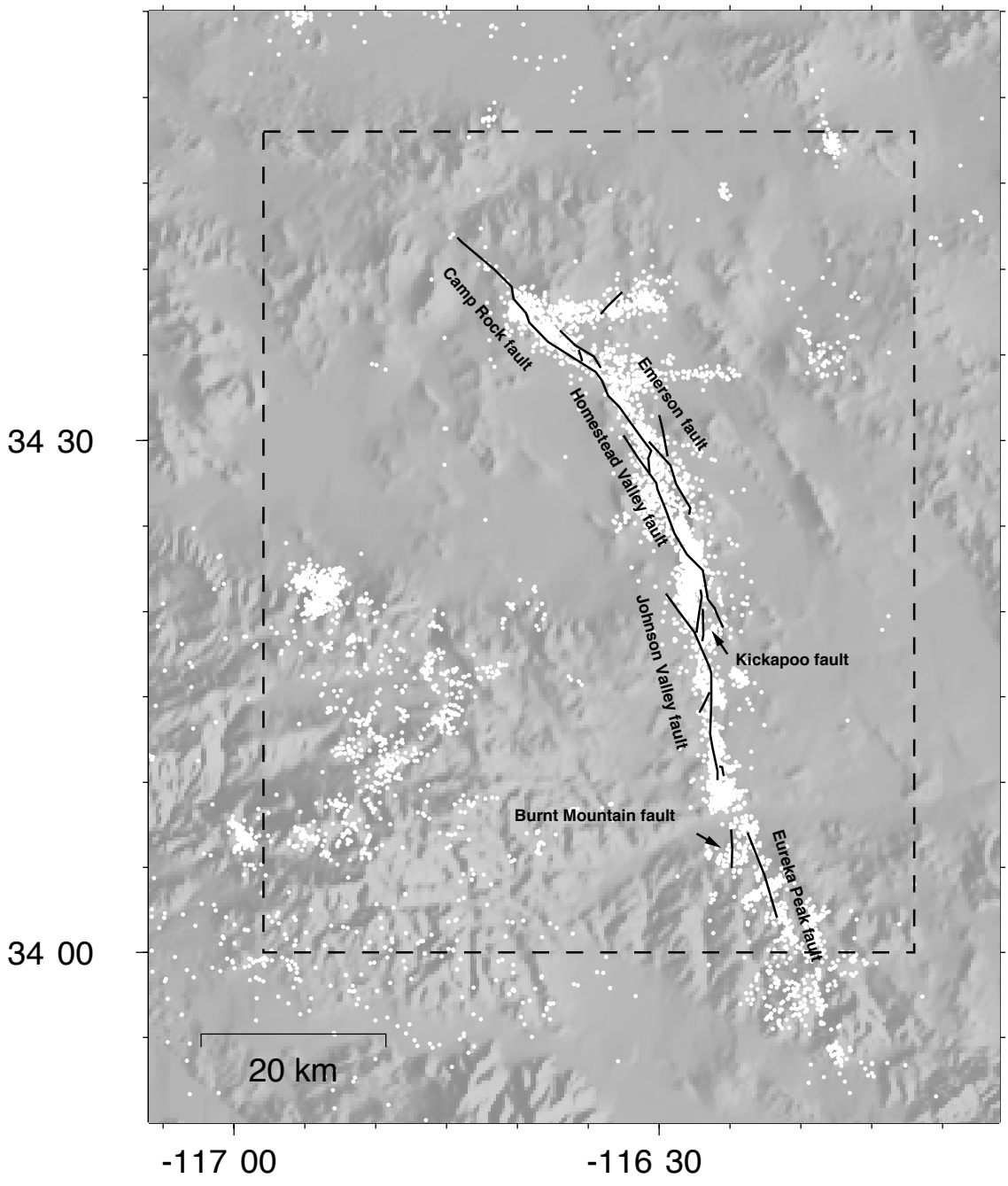
Camp Rock fault
Emerson fault
Homestead Valley fault
Johnson Valley fault
Kickapoo fault
Burnt Mountain fault
Eureka Peak fault
20 km
34 30
34 00
-117 00
-116 30

Figure 3

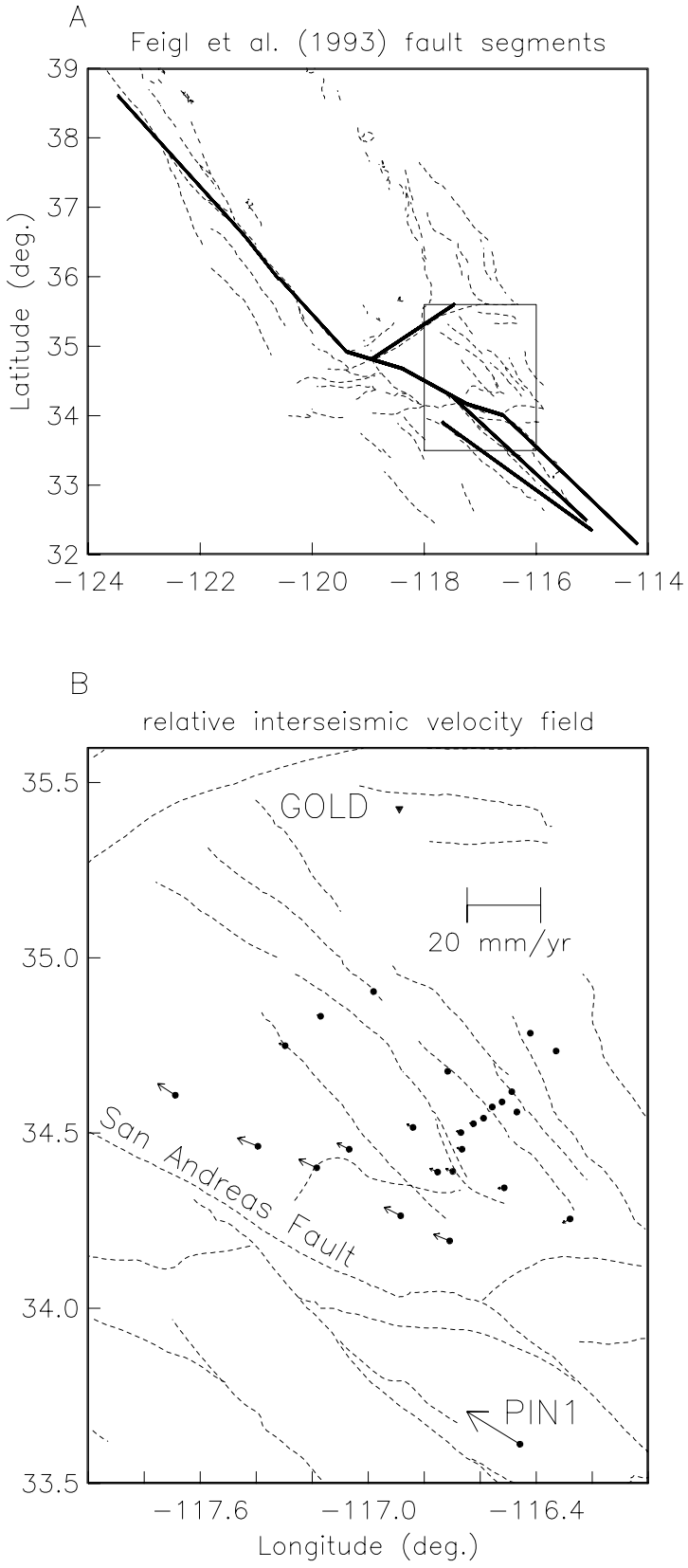
A
Feigl et al. (1993) fault segments
Latitude (deg.)
39
38
37
36
35
34
33
32
−124
−122
−120
−118
−116
−114
B
relative interseismic velocity field
35.5
35.0
34.5
34.0
33.5
GOLD
20 mm/yr
San Andreas Fault
PIN1
−117.6
−117.0
−116.4
Longitude (deg.)

Figure 4

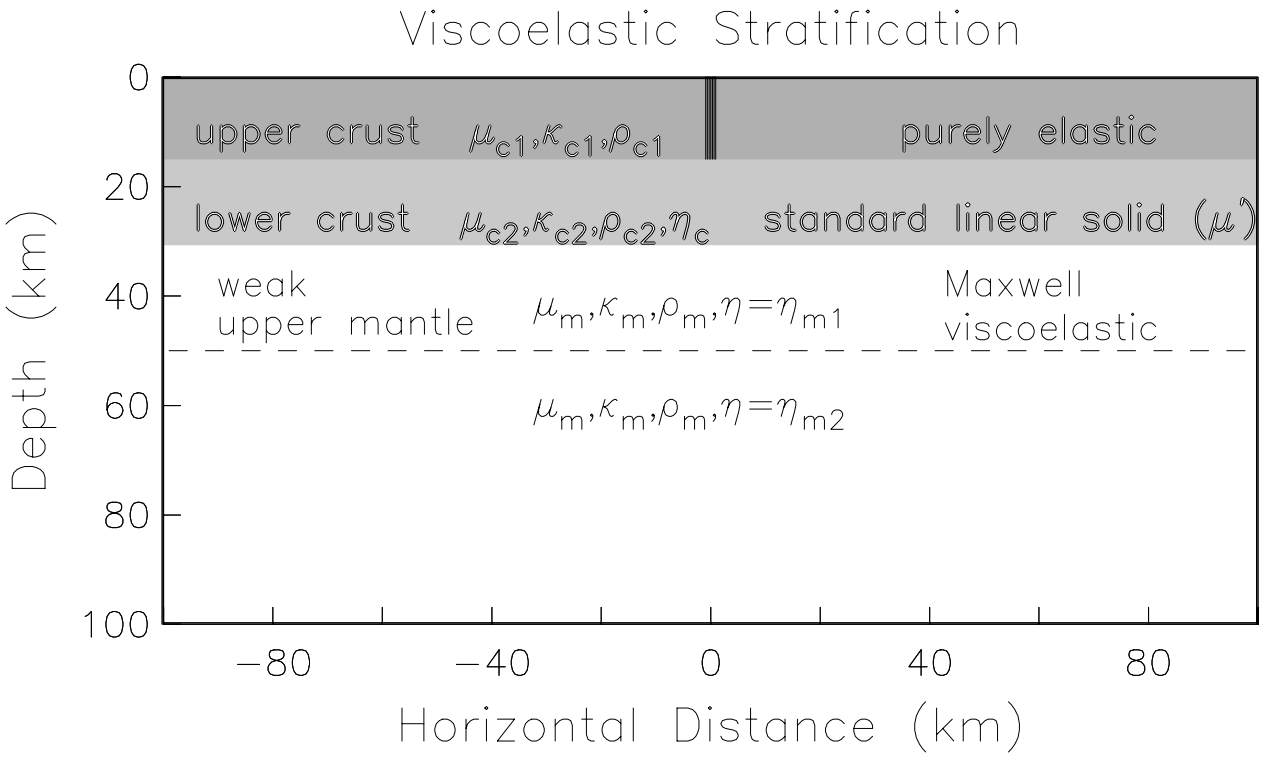
Viscoelastic Stratification
upper crust $\mu_{c1},\kappa_{c1},\rho_{c1}$
purely elastic
lower crust $\mu_{c2},\kappa_{c2},\rho_{c2},\eta_c$
standard linear solid (μ')
weak upper mantle
$\mu_m,\kappa_m,\rho_m,\eta=\eta_{m1}$
Maxwell viscoelastic
$\mu_m,\kappa_m,\rho_m,\eta=\eta_{m2}$
Depth (km)
0
20
40
60
80
100
−80
−40
0
40
80
Horizontal Distance (km)

Figure 5

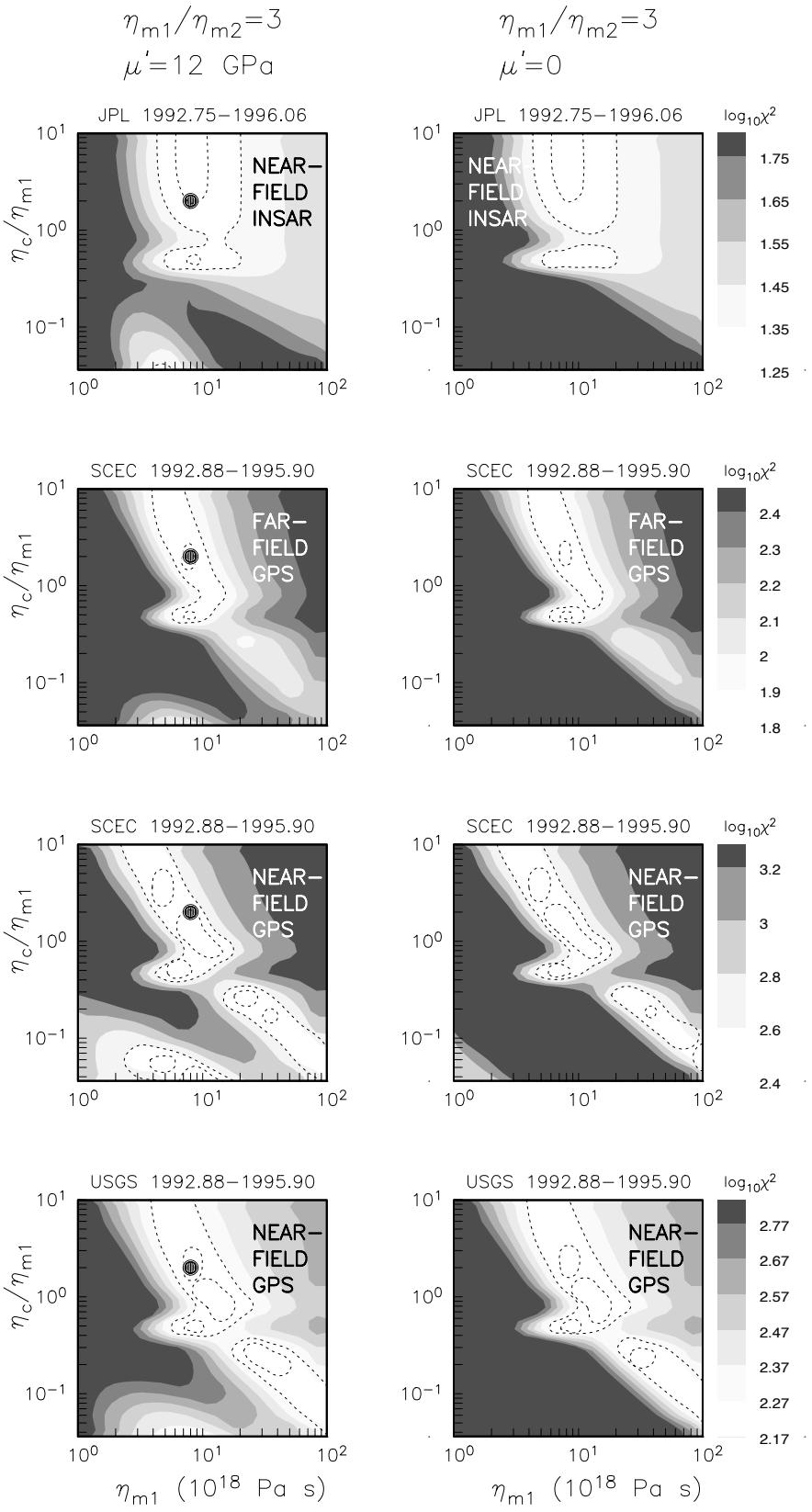
$\eta_{m1}/\eta_{m2}=3$
$\mu'=12$ GPa
$\eta_{m1}/\eta_{m2}=3$
$\mu'=0$
JPL 1992.75–1996.06
NEAR–FIELD INSAR
$\log_{10}\chi^2$
1.75
1.65
1.55
1.45
1.35
1.25
SCEC 1992.88–1995.90
FAR–FIELD GPS
2.4
2.3
2.2
2.1
2
1.9
1.8
SCEC 1992.88–1995.90
NEAR–FIELD GPS
3.2
3
2.8
2.6
2.4
USGS 1992.88–1995.90
NEAR–FIELD GPS
2.77
2.67
2.57
2.47
2.37
2.27
2.17
η_c/η_{m1}
10^1
10^0
10^{-1}
10^0
10^1
10^2
η_{m1} (10^{18} Pa s)

Figure 6

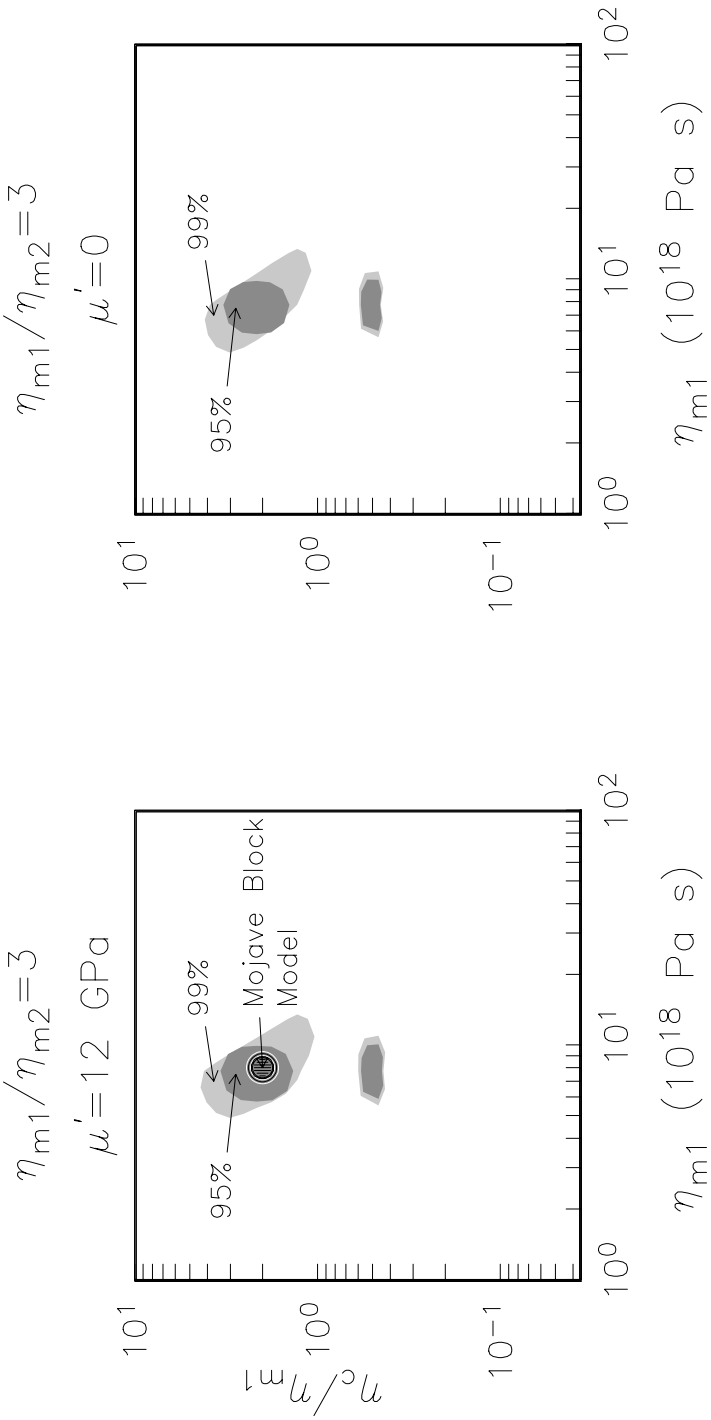
$\eta_{m1}/\eta_{m2}=3$
$\mu'=12$ GPa
$\mu'=0$
99%
95%
Mojave Block Model
η_c/η_{m1}
10^1
10^0
10^{-1}
10^0
10^1
10^2
η_{m1} (10^{18} Pa s)

Figure 7

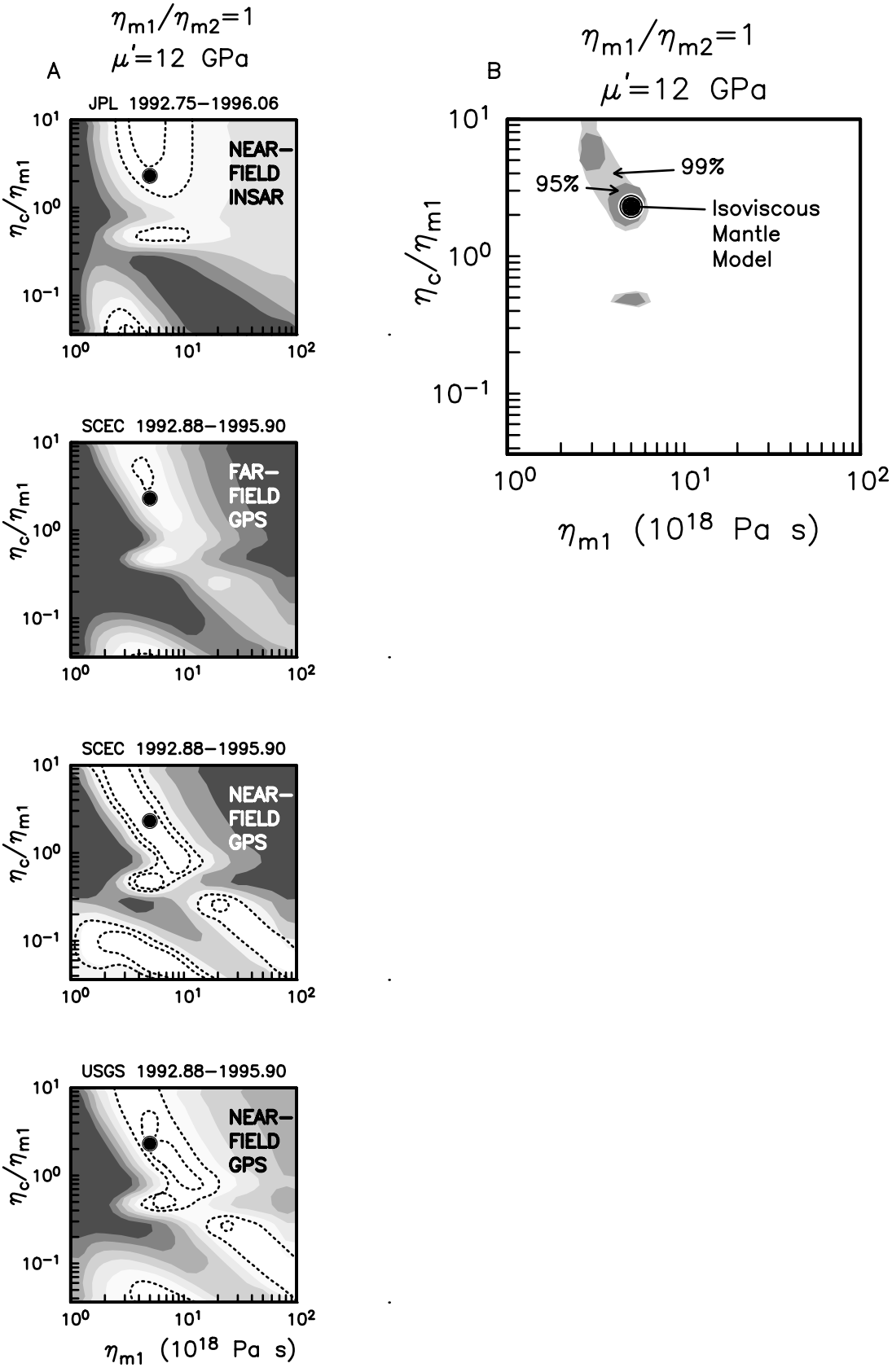
A
$\eta_{m1}/\eta_{m2}=1$
$\mu'=12$ GPa
JPL 1992.75–1996.06
NEAR-FIELD INSAR
SCEC 1992.88–1995.90
FAR-FIELD GPS
SCEC 1992.88–1995.90
NEAR-FIELD GPS
USGS 1992.88–1995.90
NEAR-FIELD GPS
η_c/η_{m1}
10^1
10^0
10^{-1}
10^0
10^1
10^2
η_{m1} (10^{18} Pa s)
B
$\eta_{m1}/\eta_{m2}=1$
$\mu'=12$ GPa
99%
95%
Isoviscous Mantle Model
η_c/η_{m1}
η_{m1} (10^{18} Pa s)

Figure 8

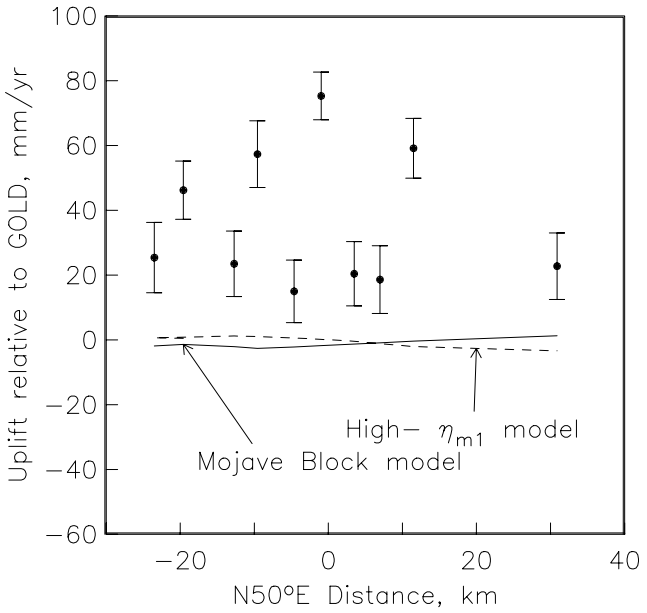
100
80
60
40
20
0
−20
−40
−60
−20
0
20
40
Uplift relative to GOLD, mm/yr
N50°E Distance, km
High− η_{m1} model
Mojave Block model

Figure 9

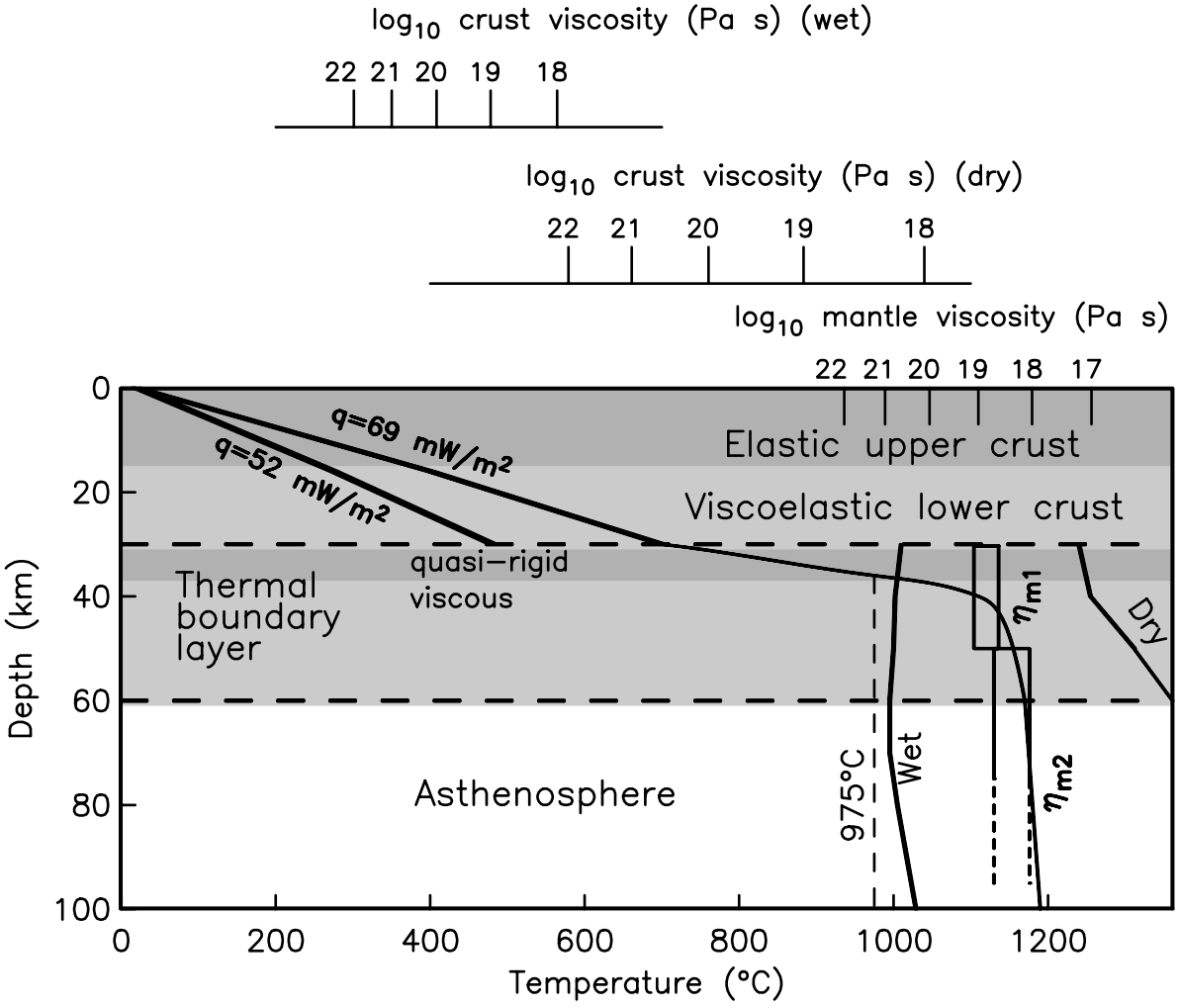
log10 crust viscosity (Pa s) (wet)
22 21 20 19 18
log10 crust viscosity (Pa s) (dry)
22 21 20 19 18
log10 mantle viscosity (Pa s)
22 21 20 19 18 17
q=69 mW/m2
q=52 mW/m2
Elastic upper crust
Viscoelastic lower crust
quasi–rigid viscous
Thermal boundary layer
Asthenosphere
ηm1
ηm2
Dry
Wet
975°C
Depth (km)
0
20
40
60
80
100
0
200
400
600
800
1000
1200
Temperature (°C)

Plate 1

Range Change (Observed)

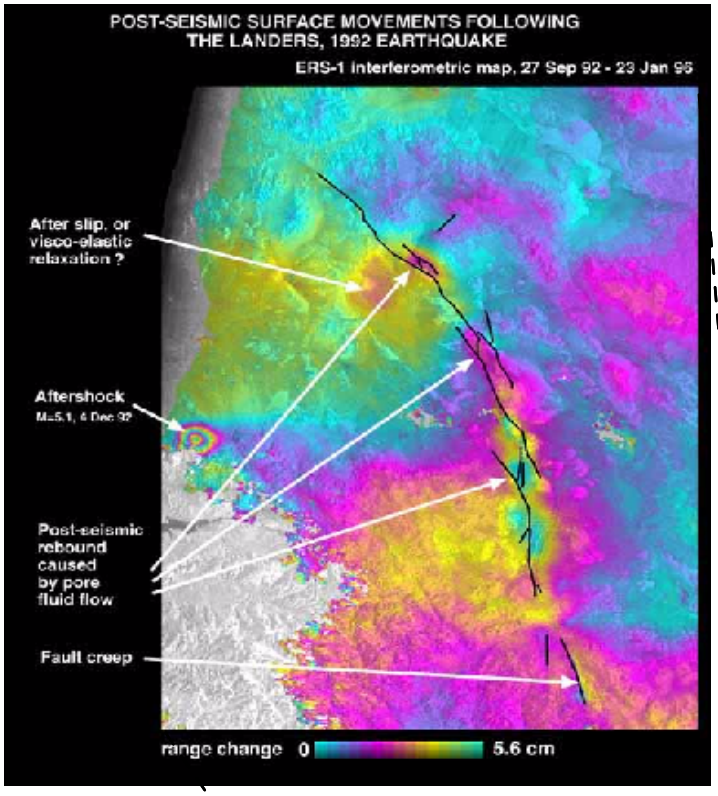

Range Change (Calculated)

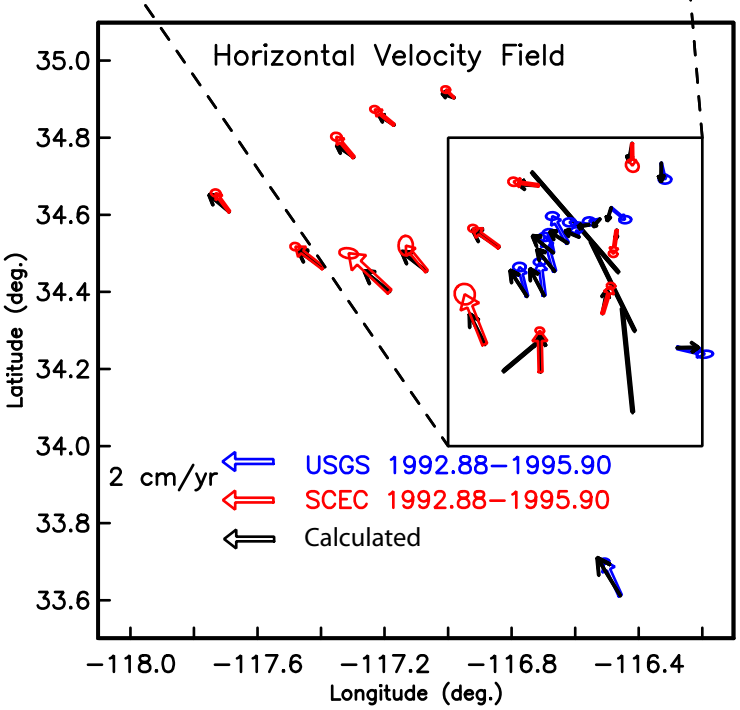

Plate 2

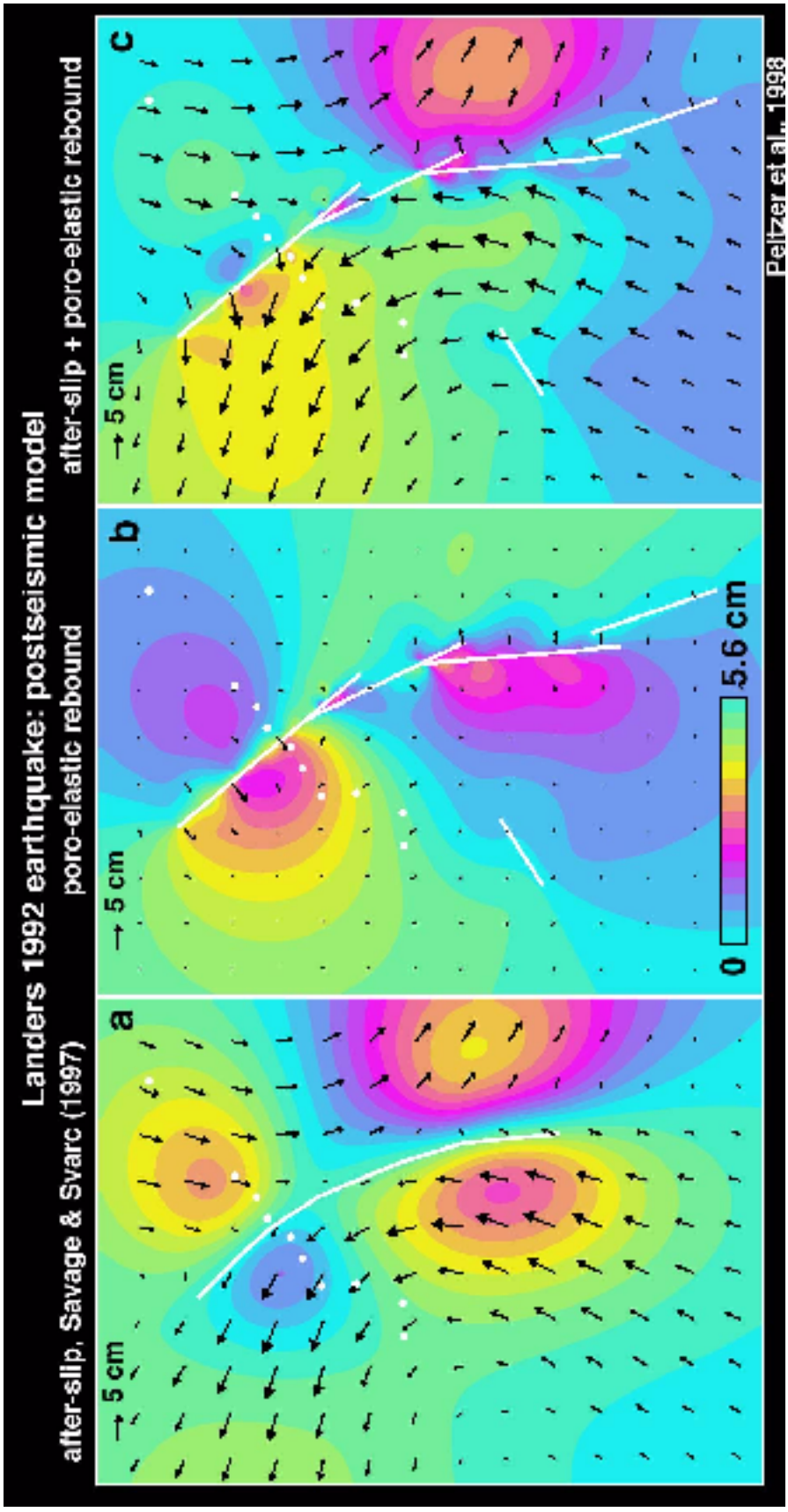
Landers 1992 earthquake: postseismic model
after-slip, Savage & Svarc (1997)
poro-elastic rebound
after-slip + poro-elastic rebound
a
b
c
5 cm
5 cm
5 cm
0
5.6 cm
Peltzer et al., 1998

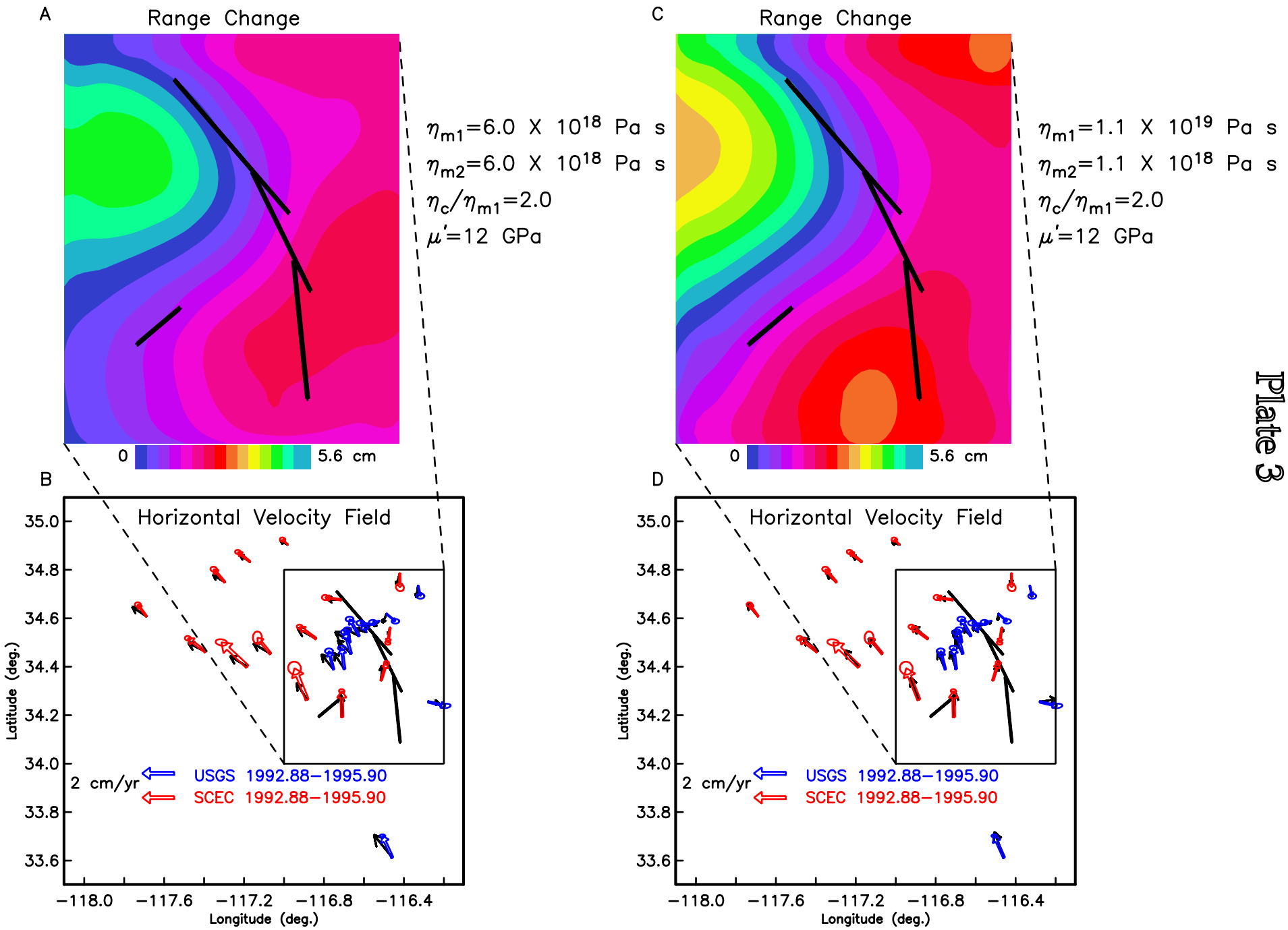
A
Range Change
η_{m1}=6.0 X 10^{18} Pa s
η_{m2}=6.0 X 10^{18} Pa s
η_c/η_{m1}=2.0
μ'=12 GPa
0
5.6 cm
B
Horizontal Velocity Field
35.0
34.8
34.6
34.4
34.2
34.0
33.8
33.6
Latitude (deg.)
−118.0
−117.6
−117.2
−116.8
−116.4
Longitude (deg.)
2 cm/yr
USGS 1992.88−1995.90
SCEC 1992.88−1995.90
C
Range Change
η_{m1}=1.1 X 10^{19} Pa s
η_{m2}=1.1 X 10^{18} Pa s
η_c/η_{m1}=2.0
μ'=12 GPa
0
5.6 cm
D
Horizontal Velocity Field
35.0
34.8
34.6
34.4
34.2
34.0
33.8
33.6
Latitude (deg.)
−118.0
−117.6
−117.2
−116.8
−116.4
Longitude (deg.)
2 cm/yr
USGS 1992.88−1995.90
SCEC 1992.88−1995.90

Plate 3

Plate 4

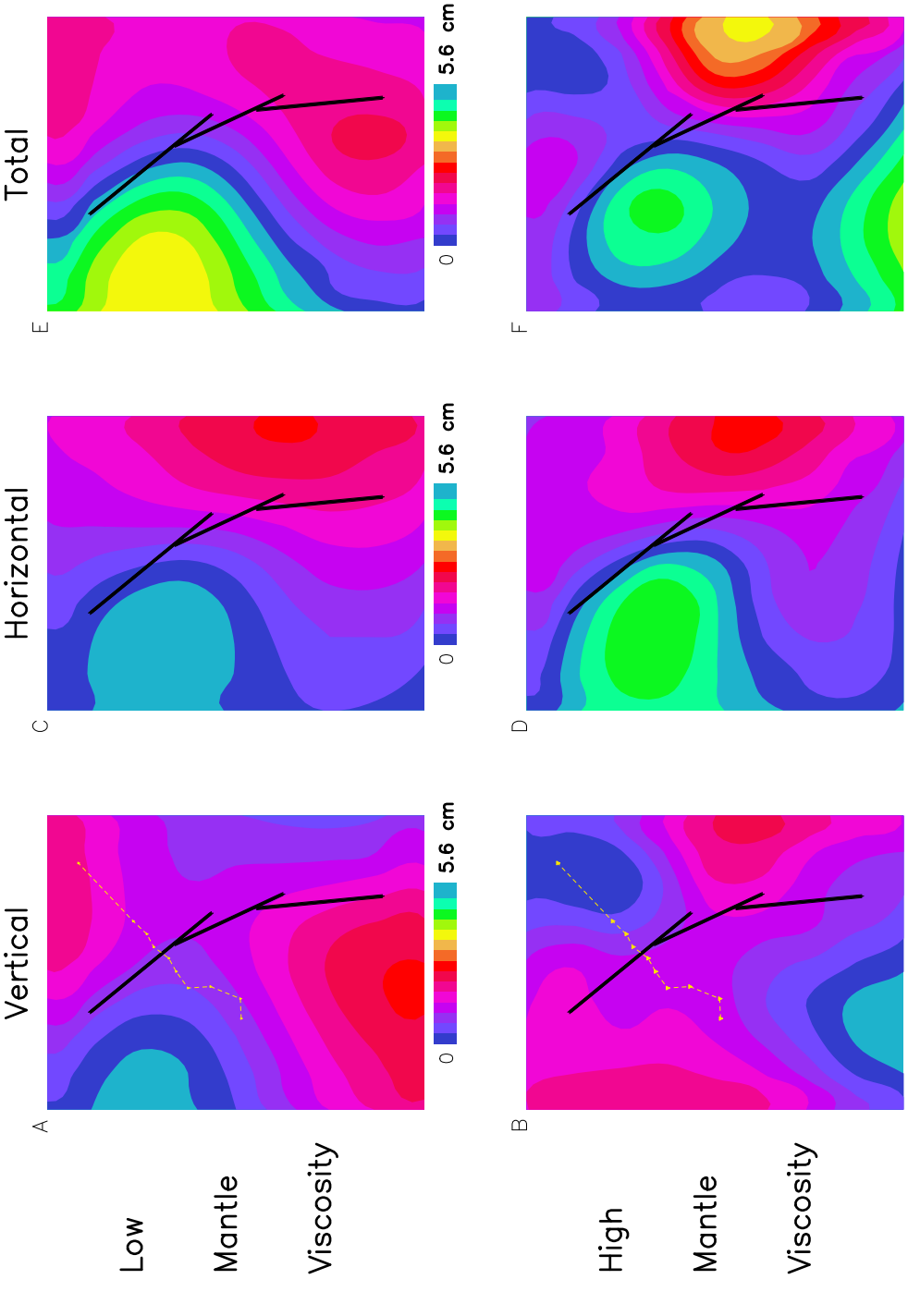
Vertical
Horizontal
Total
A
B
C
D
E
F
0
5.6 cm
0
5.6 cm
0
5.6 cm
Low
Mantle
Viscosity
High
Mantle
Viscosity